Characterizing dynamic wetting behaviour on irregularly roughened surfaces

by

©Justin Elms

A thesis submitted to the School of Graduate Studies in partial fulfillment of the requirements for the degree of

Master of Science

Department of Physics and Physical Oceanography

Memorial University of Newfoundland

September 2018

St. John's Newfoundland

Abstract

Surface wettability describes the behavior of liquids on substrates and their ability to remain in contact with them. Quantification of wettability is often reduced to a measurement of the contact angle that a liquid droplet makes on the surface. Although this practice has become ubiquitous in the literature, a growing number of researchers have voiced concerns that static contact angles alone cannot fully describe surface wetting properties. Our research findings fall in line with this sentiment and highlight some of the difficulties encountered when quantifying dynamic wetting behavior. The wetting dynamics of more than 300 droplets were studied on randomly roughened surfaces to demonstrate the range over which advancing and receding contact angles can vary. Factors such as droplet size, rate of volume change, and shape fitting algorithms affected measured contact angles. The relation between static and dynamic contact angle data was compared based on empirical models developed by others [Furmidge *J. Colloid Sci.*, 1962, **17**(4), 309; Xiu *et al.*, *J. Phys. Chem. C*, 2008, **112**(30), 11403]. The results of these comparisons demonstrate that static contact angles alone are not enough to characterize irregularly roughened surfaces, and that more information related to dynamic wetting behavior, such as sliding angles and hysteresis, is essential.

Acknowledgements

My thanks and appreciation to my supervisor, Dr. Kristin Poduska and the members, past and present, of the Poduska Research group for their support and guidance throughout this project. I would also like to thank Dr. Xili Duan and the members of his research group for their insight and fruitful discussion.

Thank you to Terri and the rest of my family and friends for their continuous support throughout this program. I could not of accomplished this without them.

Lastly, my sincere appreciation to Petroleum Research Newfoundland & Labrador, the Department of Physics and Physical Oceanography, and the School of Graduate Studies for their financial support.

Table of Contents

Abstract ii

Acknowledgments iii

Table of Contents vi

List of Tables vii

List of Figures x

1 Introduction 1

2 Background: Wetting Models, Surface Roughness, Contact Angle Hysteresis, and Contact Line Pinning 4

2.1 Surface Wetting Models 4

2.2 The Effect of Roughness on Wetting 8

2.3 Contact Angle Hysteresis 9

2.3.1 Hysteresis and the Sliding Angle 10

2.3.2 Hysteresis and the Work of Adhesion 11

2.4 Pinning of the Contact Line 11

2.5 Hysteresis Throughout the Literature 13

3 Experimental Methods **15**

3.1 Surface Preparation 15

3.1.1 Sandblasted Surfaces 15

3.1.2 Sanded Surfaces 16

3.1.3 Wax Surfaces 16

3.2 Contact Angle Measurements 17

3.2.1 Static Contact Angle Measurement 17

3.2.2 Dynamic Contact Angle Measurement 18

4 Dynamics of Droplets on Roughened Surfaces **20**

4.1 Outline of the Experiment 21

4.2 Refining the Dynamic Measurement Method 22

4.2.1 Fitting Methods 23

4.2.2 Asymmetry 25

4.2.3 Actual Volume *vs.* Calculated Volume 27

4.2.4 Measurement Rate 29

4.3 Dynamic Measurements on Irregularly Roughened Surfaces 31

4.3.1 Droplet Size Effects on Sandblasted Stainless Steel 32

4.3.2 Dosing Rate Effects on Sandblasted Stainless Steel 33

4.4 Summary of Findings 34

5 Surface Pinning: Looking Ahead **36**

5.1 Challenges in Characterizing the Pinning Length Scale 36

5.2 The Effect of Measurement Rate on Discontinuities 37

5.3 Assessing Pinning Length Scales 39

5.3.1 Presenting Pinning Information 42

5.4 Summary 43

6 Conclusions **45**

A Equipment Used **47**

A.1 Contact Angle Measuring Instrument OCA 15EC 47

Bibliography **48**

List of Tables

4.1 Comparison of acceptable measurements, as a function of data fitting rates, during dynamic CA measurements. 30

4.2 Maximum and minimum advancing and receding contact angles observed, mean contact angle hysteresis, mean observed sliding angle, and mean calculated sliding angle for the tested surfaces. All measurements have units of degrees. 31

4.3 Comparison of droplet volume effects on data acceptability during dynamic CA measurements. 33

4.4 Analysis of dosing rate effects during dynamic CA measurements. . . 34

List of Figures

2.1 Schematic diagram of a static contact angle (θ_{ideal}) on an ideal surface. 5

2.2 Methods of inducing contact angle hysteresis on a surface. 9

4.1 Dynamic contact angle and volume measurements on a sandblasted stainless steel surface. 21

4.2 Two typical dynamic contact angle measurements (red and blue) for tested surfaces. Droplet size was 20 µL, and dosing rate was 2 µL·s^{-1}. 22

4.3 Comparison of the baseline (1), contour fit (2), and contact angles (3) produced by elliptical and polynomial fitting of the same droplet during a dynamic contact angle measurement. 23

4.4 Dynamic droplet characterization using both polynomial (blue) and elliptical fits (red). Droplet volume was initially 20 µL, and increased at with a 2 µLs^{-1} dosing rate, then decreased at the same rate. 24

4.5 Polynomial contour fitting during the receding phase of a dynamic contact angle measurement. 25

4.6 Asymmetry of a 20 µL droplet during the advancing phase of dynamic contact angle measurement at a 2 µLs^{-1} rate. 26

4.7 Left (red), right (blue), and mean (green) dynamic contact angle measurements representative of 30 μL droplets at a rate of 2 μLs^{-1} with asymmetries occurring at the beginning, (a), and end, (b), of measurement. 26

4.8 Left and right contact line positions (left column), contact angles (centre column), and volume data (right column) for 20 μL drops dispensed at 2 μLs^{-1}. Measurement rates vary from 1 (top row) to 5 (bottom row) measurements per second. 28

4.9 Calculated volume change (blue) of two different representative 20 μL drops during dynamic measurements with a volume change rate of 0.2 μLs^{-1}. (a) shows a good fit (smooth volume changes), while (b) shows a bad fit. 29

4.10 Histograms of RMS contour fitting error from acceptable and unacceptable dynamic contact angle measurements. 30

4.11 Left (red), right (blue), and mean (green) dynamic contact angle measurements of 5 μL droplets, whose volumes were changed at a rate of 2 μLs^{-1}. 32

4.12 Left (red), right (blue), and mean (green) dynamic contact angle measurements of 10 μL droplets, whose volumes were changed at a rate of 2 μLs^{-1}. 32

4.13 Left (red), right (blue), and mean (green) dynamic contact angle measurements of 20 μL droplets, whose volumes were changed at a rate of 2 μLs^{-1}. 33

4.14 Left (red), right (blue), and mean (green) dynamic contact angle measurements of 30 μL droplets, whose volumes were changed at a rate of 2 μLs^{-1}. 33

5.1 Dynamic contact angle and base diameter measurement of a 20 μL droplet. Each point of the base diameter curve was produced by a separate automatic fit to a droplet image extracted from a video. . . 38

5.2 Frames 156 - 163 of the dynamic contact angle measurement video data referenced in Figure 5.1. The software's algorithm automatically fits the droplet shape well at frame 156 (a). However, the contact line moves far beyond the fit (b-g) before the next fit is applied at frame 163 (h). 38

5.3 Histograms of pinned droplet diameter changes on sandblasted stainless steel for 20 μL drops during dynamic contact angle measurements. Dosing rates were 2 $\mu L \cdot s^{-1}$. The measurement rate varied from 1 to 10 measurements per second. 40

5.4 The pinned droplet diameter values for 20 μL droplets on sandblasted stainless steel. Dosing rate was 2 $\mu L \cdot s^{-1}$, with 1-10 measurements per second. 40

5.5 Dynamic contact angle measurement of 20 μL drop on sandblasted stainless steel surface, with a dosing rate of 2 $\mu L \cdot s^{-1}$. 41

5.6 Comparison of three histogram methods 43

5.7 Average shifted histogram of pinned droplet diameters on sandblasted stainless steel for a 20 μL drop during dynamic contact angle measurements. The dosing rate was 2 $\mu L \cdot s^{-1}$. 44

List of Abbreviations and Symbols

α	sliding angle
$\Delta\theta$	contact angle hysteresis
γ_{LS}	liquid-solid surface tension
γ_{LV}	liquid-vapour surface tension
γ_{SV}	solid-vapour surface tension
ϕ_{LS}	liquid-solid surface fraction
ϕ_{LV}	liquid-vapour surface fraction
θ_a	apparent contact angle
θ_A	advancing contact angle
θ_A^*	intrinsic advancing contact angle
θ_{ideal}	ideal contact angle
θ_{LS}	liquid-solid contact angle
θ_{LV}	liquid-vapour contact angle
θ_R	receding contact angle
θ_R^*	intrinsic receding contact angle
Θ	asperity inclination

AFAP	as-fast-as-possible measurement rate
ARCA	advancing & receding contact angle
ASH	average shifted histogram
CA	contact angle
g	gravitational constant
m	mass
SS	stainless steel
w	drop interface width
W_{ad}	work of adhesion

Chapter 1

Introduction

Surface wettability describes a liquid's ability to maintain contact with a solid surface. Water droplets on a polymer surface bead up and glide over the surface. On a metal, the same water droplet will spread, completely wetting the surface. These behaviours are due to the difference between surface energies of these materials. A material whose surface has a high water affinity is deemed hydrophilic and low affinity surfaces are hydrophobic. [1–3] Low energy surfaces such as Teflon are hydrophobic while a surface with high energy, such as stainless steel, is inherently hydrophilic. Such effects are studied in many disciplines of science due to the vast number of applications for these behaviors, including self-cleaning and water repellent surfaces. [1–7] Examples include everyday use applications such as: clothing items that repel water to prevent stains, protecting concrete from water seepage, and waterproof paints. [2, 4, 8, 9] In industry, wetting and spreading processes are utilized in lubrication, adhesion, painting, spray quenching and soldering. [10] Water repellent surfaces are also used in medicine where they help prevent the fouling of medical devices. [8] In many of these applications, the surface of the material is treated with coatings, such as paint, that modify the surface energy to achieve the desired wetting effect. [1, 2, 9–12]

Non-wetting surfaces can also be produced through roughening. [1, 2, 4, 5, 10, 11, 13–16] Rough surfaces allow air to become trapped between the solid and water which results in hydrophobic behavior. A great deal of work has gone into developing regularly patterned surface structures that are superhydrophobic. [2, 6, 17] These surfaces have roughness features that are placed periodically in a precise array, and can be produced from a variety of materials such fluorocarbons, silicon, copper, and zinc. [2, 3, 9, 16, 18, 19] Materials with low surface energies, such as metals, must use a combination of coatings and roughness to achieve superhydrophobic properties. [9, 10, 16, 20, 21]

The research presented in this dissertation is a part of a larger project to produce and characterize hydrophobic surfaces for large-scale marine applications in order to reduce corrosion and ice accretion on offshore assets. For this application, hydrophobic coatings and paints are not viable as they wear off quickly in the harsh marine environment and are difficult to repair. The research goal is to explore whether roughened surfaces will promote sufficient water repellency. While regularly patterned surfaces have been shown to be effective in repelling water, they cannot be easily produced on industrial scales. [16] This is due to limitations of the micro-fabrication techniques used to produce regularly patterned surfaces. Because of this, we focus on surfaces roughened using sandblasting and sanding techniques that are much easier to apply on a large scale, and have not been studied as extensively in the literature. [10] The intent of my thesis work is to characterize the dynamic water wetting behavior of sanded and sandblasted surfaces.

In the following chapter, simple models used to describe surface wetting and adhesion will be explored. These models are widely used to quantify and predict contact angles, adhesion, pinning, and sliding angles. In Chapter 3, the techniques used to prepare and characterize the rough surfaces are presented. Chapter 4 delves into the

experimental results, focused on a critical analysis of dynamic contact angle measurement. Observations made throughout these measurements lead to the proposal of another characterization method discussed in Chapter 5. In Chapter 6, the results of this thesis work and plans for future research are summarized.

Chapter 2

Background: Wetting Models, Surface Roughness, Contact Angle Hysteresis, and Contact Line Pinning

2.1 Surface Wetting Models

In simple terms, surface wetting is the ability of a liquid droplet to remain in contact with a solid surface. It is well-established that, for ideal surfaces, this phenomenon is characterized by the Young angle (θ_{ideal}) which is dependent on the surface (interfacial) tensions (γ) as seen in Equation 2.1. Here, γ_{SV} is the solid-vapor interfacial tension, γ_{SL} the solid-liquid tension, and γ_{LV} the liquid-vapor tension. [1, 22–25] This angle between the surface of the droplet and the solid substrate indicates that a surface is hydrophilic when $\theta < 90°$, and hydrophobic when $\theta > 90°$. [23]

$$\cos\theta_{ideal} = \left(\frac{\gamma_{SV} - \gamma_{SL}}{\gamma_{LV}}\right) \tag{2.1}$$

The apparent contact angle given by traditional models is usually experimentally unobtainable. Even smooth, simple surfaces have been shown to have various contact angles. [1, 4, 26] Such deviations may arise from long-range interactions between molecules forming the triple line of the droplet, and the molecules forming the solid substrate. Contact angles also change over time. It has been shown that the observed angle can change due to re-orientation of water molecules. [22]

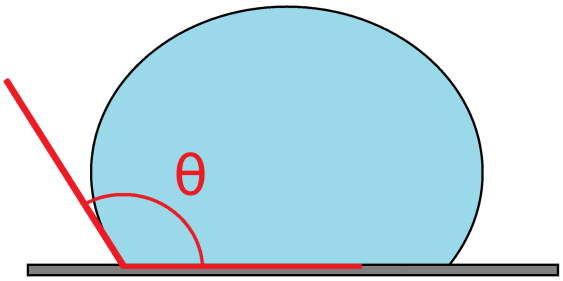

Figure 2.1: Schematic diagram of a static contact angle (θ_{ideal}) on an ideal surface.

Contact angles around the perimeter of a liquid drop are not typically uniform. Thus, a single unique contact angle may not be sufficient to characterize a given substrate. [2] However, surface repellency can also be characterized by the dynamics of a liquid droplet. The rolling-off (sliding) behavior of liquid droplets can also be used to quantify the wettability of a surface. Water droplets often have difficulty sliding off a surface with a large static contact angle due to a phenomenon known as contact angle hysteresis. [14]

Throughout the literature, surface wetting is described using two models: the Wenzel and Cassie-Baxter models. [2,11,27–29] These one-dimensional models assume that the liquid's contact angle is a function of surface geometry. Wenzel's theory is based on the assumption that a rough surface extends the solid-liquid interface area

compared to the projected smooth surface. In this model, the liquid is in continuous contact with the substrate and its apparent contact angle, θ_a, is given by Wenzel's equation (Equation 2.2). Here, r is proportional to the increase in surface area due to the roughness, and θ_{ideal} is the contact angle of the idealized surface. In practice, Wenzel's theory applies best to hydrophilic surfaces where the contact angle range is $0° < \theta < 90°$. [10] Thus, Wenzel's relation shows that surface roughness will decrease the contact angle for a droplet on a hydrophilic surface and increase the contact angle for a droplet on a hydrophobic surface. [23]

$$\cos\theta_a = r\cos\theta_{ideal} \tag{2.2}$$

The Cassie-Baxter model describes the apparent contact angle for a composite material, as described by Equation 2.3. The model describes a liquid drop resting on a rough surface. Cassie and Baxter assumed that if thin, deep channels are present on a hydrophobic surface, a water droplet resting on the surface will not enter the channels. On these surfaces, a liquid drop effectively sits upon a composite surface of the solid protuberances and air. [16] As in Wenzel's model, θ_a and θ_{ideal} are the apparent and ideal contact angles. The ϕ_{LS} and ϕ_{LV} terms are the liquid-solid and liquid-vapour area fractions of each component while θ_{LS}, and θ_{LV} are the corresponding contact angles. [10] When dealing with a system where the vapour component is air, $\theta_{LV} = 180°$ and $\phi_{LV} = 1 - \phi_{LS}$. The model then takes the form of Equation 2.4.

$$\cos\theta_a = \phi_{LS}\cos\theta_{LS} + \phi_{LV}\cos\theta_{LV} \tag{2.3}$$

$$\cos\theta_a = \phi_{LS}(\cos\theta + 1) - 1 \tag{2.4}$$

The apparent contact angle is influenced by the area fraction, ϕ_{LS}, of the droplet

in contact with the surface. High apparent contact angles are characteristic of the Cassie-Baxter model, and so the model is commonly used to describe hydrophobic surfaces ($90° < \theta < 180°$). [22]

Improving wetting characteristics as per Wenzel's equation calls for an increase in effective surface area, whereas Cassie's equation calls for a sufficient aspect ratio that the fluid cannot penetrate. [16] However, a droplet initially described by one of them is not confined to remain in that state forever. [10] Droplets are able to transition between the two states under the right circumstances. More recent work has built upon the Cassie-Baxter and Wenzel models in an effort to calculate sliding angles and the work of adhesion for surfaces. [21, 30, 31]

Much of today's literature uses the Wenzel and Cassie-Baxter models to understand and manipulate a surface's wetting properties with the intent of creating superhydrophobic surfaces through physically and chemically modifying their surface. A rough patterned or porous surface can be created in order to enhance the material's wetting properties. [16] Many studies focus on the contact angle a droplet makes on the resulting surface. [6, 9, 14, 16, 32, 33] This makes for a quick assessment to compare these surfaces. However, a lot of valuable information can be neglected. For example, a surface can exhibit high contact angles while having high water adhesion. Though this kind of surface is not water repellent, contact angle measurements would lead one to believe it is hydrophobic. This has led to literature that makes a strong case that other important factors in the study of wetting behavior, such as contact angle hysteresis and contact line pinning, receive too little attention. [27] These elements contribute to water adhesion and sliding angles of substrates which is of great importance in many applications.

2.2 The Effect of Roughness on Wetting

The impact of roughness on the wettability of a solid substrate is well known and documented frequently throughout the literature. [10, 13, 25, 34] Surface roughness, as observed by Wenzel, appeared to have a greater effect on the static contact angle than surface chemistry. [35] Roughness alone can cause a hydrophobic material to behave as if it were more hydrophobic, and can cause a hydrophilic material to behave as if it were more hydrophilic. [36] The lotus leaf, perhaps the most famous example of hydrophobicity, is inherently hydrophilic. The leaf's hydrophobic properties are almost entirely due to its surface roughness geometry. [24] Other studies found similar results in the dynamics of liquids spreading on smooth and rough surfaces.

Much recent literature focuses on manufactured substrates on which roughness is created by placing asperities on the surface through a variety of methods. These features are often pillars of various sizes and spacing. The size and placement of such pillars are quantified by the surface fraction ϕ_{LS} as used in the Cassie-Baxter model (Equation 2.4). [1,2] Because increasing the number of asperities allows more air to be trapped underneath a liquid drop, rougher surfaces are frequently associated with the Cassie-Baxter state. Even if the surface is constructed of pillars with low roughness, the Cassie-Baxter state is normally observed.

From the Wenzel and Cassie-Baxter models, the apparent contact angle increases monotonically as ϕ_{LS} decreases, suggesting that more hydrophobic surfaces would have smaller ϕ_{LS}. As ϕ_{LS} is directly related to roughness, this would result in a surface that favors the Wenzel state. [2] Other experimental results show that there is a critical density of roughness features, below which there is a deterioration of water-repellent properties. [2,25] The minimum texture size that promotes water repellency, and the mechanisms behind the loss of hydrophobicity, are still unknown. [2]

2.3 Contact Angle Hysteresis

Contact angle hysteresis tends to be greater on rougher surfaces, but chemical interactions and heterogeneities also contribute to this effect. [10] Measured static contact angles for a given surface will lie in a range $\Delta\theta$, the contact angle hysteresis. Hysteresis is often defined as the difference between the advancing contact angle at the leading edge of the contact line, θ_A, and the receding contact angle at the trailing edge, θ_R. [4,26] Although hysteresis makes the Young angle difficult to ascertain, it is used to help define the water-surface interaction. For example, the combination of a very large contact angle (>150°) and low contact-angle hysteresis is characteristic of a superhydrophobic surface. [22,37] Superhydrophobicity is usually observed in droplets in motion on a surface, and it is strongly related to the surface's sliding angle and work of adhesion W_{ad}.

In the laboratory, contact angle hysteresis is measurable in two scenarios as shown in Figure 2.2. With the sliding droplet method (Figure 2.2a), the surface is tilted until the droplet begins to slide, at which point θ_A and θ_R are measured. Hysteresis can also be observed while modifying the droplet's volume (Figure 2.2b). As the volume increases, the contact angle increases until θ_A can be measured. Likewise, as volume decreases, θ_R can be measured.

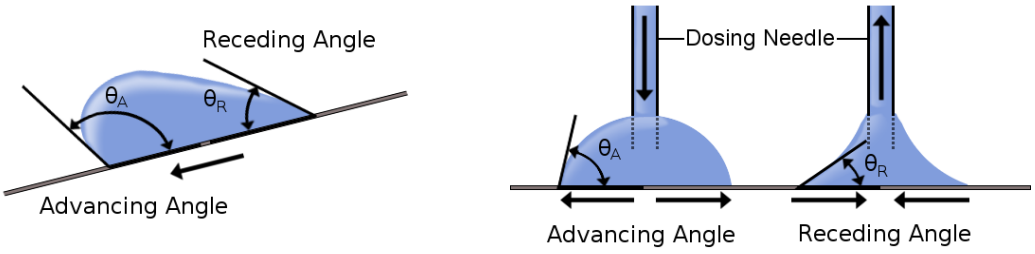

(a) Sliding drop method. (b) Volume modification method.

Figure 2.2: Methods of inducing contact angle hysteresis on a surface.

2.3.1 Hysteresis and the Sliding Angle

In the study of wettability, sliding angle is the angle at which a surface must be tilted in order for a liquid drop to roll off, and it is commonly used to quantify surface wetting. In general, a droplet in the Wenzel state will remain static even if the substrate is tilted to a significantly steep angle. A droplet in the Cassie-Baxter state will slide at shallower angles. The sliding behavior of a liquid droplet is also governed by the movement of the three-phase contact line toward its sliding direction. A short continuous contact line is favorable for producing a low sliding angle or low contact angle hysteresis. [14]

Furmidge noticed that a droplet's resistance to movement on a surface was related to hysteresis. [4,27,30] He deduced that the work done in wetting a unit area of a solid surface is equal to $\gamma_{LV}(1+\cos\theta_A)$, while the work done in dewetting a unit surface is $\gamma_{LV}(1+\cos\theta_R)$. [30] The total work done by a drop moving a distance dl is equivalent to the difference of these functions and can be expressed as:

$$mg\sin\alpha\ dl = \gamma_{LV} w\ dl\cos\theta_R - \gamma_{LV} w\ dl\cos\theta_A. \tag{2.5}$$

Here, $mg\sin\alpha$ is the force that causes the drop to move, w is the drop width, γ_{LV} is the liquid-vapour surface tension, and $\cos\theta_R - \cos\theta_A$ is an alternate interpretation of hysteresis. The work done during the sliding is equal to $mg\sin\alpha dl$, where dl is the distance travelled by the drop. [30] Simplifying this relation gives Furmidge's relation, Equation 2.6.

$$\frac{mg\sin\alpha}{w} = \gamma_{LV}(\cos\theta_R - \cos\theta_A). \tag{2.6}$$

2.3.2 Hysteresis and the Work of Adhesion

Work of adhesion, W_{ad}, differs from mechanical adhesion in that it describes the free energy difference between two states. [38] In simplest terms, the work of adhesion is the work that must be done to separate two phases in contact with each other. This concept is believed to be a major contributor to contact angle hysteresis. [31] W_{ad} is given by the Young-Duprè equation as:

$$W_{ad} = \gamma_{LV}(1 + \cos\theta_{ideal}). \tag{2.7}$$

It assumes that the force needed to move a water droplet on a rough surface is the force required to overcome the work of adhesion. [31] As the droplet moves, energy barriers are experienced on the receding side. The energy is equal to the work of adhesion required to separate the droplet from the surface. It can be expressed as $F\delta = W_{ad}\delta\pi R$, where δ is the distance the droplet has moved and R is the drop-surface contact radius. [31] Starting from Furmidge's relation (Equation 2.6), Xiu deduced that the work of adhesion involved in the movement of the drop is related to hysteresis by

$$(\cos\theta_R - \cos\theta_A) = \frac{\pi}{2}\phi_{LS}(1 + \cos\theta_{ideal}). \tag{2.8}$$

2.4 Pinning of the Contact Line

The dynamics of a liquid droplet's contact line are strongly influenced by the substrate on which the droplet rests. Surface heterogeneities, whether physical or chemical, can distort the contact line of a droplet as it moves, which in turn may cause the droplet to adhere to the surface. [39–43] This phenomena is referred to as contact line pinning, and it is important in many applications of hydrophobic surfaces. [40]

Pinning is commonly observed as a droplet moves across a surface. This behavior is influenced by a number of surface characteristics including surface chemistry, the number density of surface asperities, and the height and slope of these asperities relative to the mean surface plane. [40, 41, 44]

When the advancing droplet meets an asperity with inclination Θ, the local advancing line will remain pinned at its current position until the advancing contact angle becomes $\theta_A^* = \theta_A + \Theta$. [41] Likewise, once the receding line meets the asperity, it will remain pinned until the intrinsic receding angle is observed, $\theta_R^* = \theta_R - \Theta$. [41] These conditions provide the basis for the Gibbs inequality:

$$\theta_R^* = \theta_R - \Theta \leq \theta_a \leq \theta_A + \Theta = \theta_A^*. \tag{2.9}$$

This inequality shows that the apparent contact angle, θ_a, lies in a range between the intrinsic advancing and intrinsic receding angles. The effect of defect height on pinning has been commented upon frequently throughout the literature. [41, 45–48] Many combinations of liquid-solid interactions were studied and results varied considerably. Mori *et al.* examined the spreading of oleyl alcohol and diethylene/ethylene glycols on surfaces with microsteps. [45] Their work suggests that step heights smaller than 30-50 nm would be ineffective in pinning the advancing line. In contrast, studies of liquid polystyrenes on annealed alumina surfaces show that steps with heights as small as 2-10 nm pinned the receding line. [46] Kalinin *et al.* studied pinning due to microscale topography and found that the advancing contact angle increased with feature size up to heights of ≈ 2 μm. [41] Producing surfaces with taller micro-structures did not increase θ_A. Their work also showed that the height of the asperities had a greater influence on pinning than the asperity's slope. Steeply sloped features smaller than 1 μm were ineffective in pinning the contact line. Abbott *et al.* used surface scratches (0.1 μm to 10 μm) to show that wider defects pin more strongly. [47] Others

expanded upon this by modifying surfaces with features of different widths to show that droplets pin when stepping down from high defects to the mean surface plane. [41] The slope of the sidewalls of these features, and the distance between them, affected pinning behavior. This agrees with other work that proposes that an advancing liquid engulfs the asperities until the contact line comes to a rest at the outer edges, preventing the contact line from traveling down the face of the feature. [39]

2.5 Hysteresis Throughout the Literature

The link between contact angle hysteresis and hydrophobic surface properties is well known and documented throughout the literature. [4, 26, 27] However, there is not yet a universally agreed upon explanation of this behavior. Two molecular-kinetic models, Blake and Haynes' model [49] and Cox-Voinov law [50, 51], propose that contact line motion is determined by the statistical dynamics of molecules within an area where solid, liquid, and gas meet. The former model was found to fit particularly well in regimes of high drop velocity while the later is only valid while the Reynolds and capillary numbers are less than 1. [4] Alternatively, the hydrodynamic model assumes that the moving process of the contact line is a product of the viscous dissipation of the liquid. [4] This implies that the bulk friction is the main resistance to contact line motion. Other thermodynamic models have been put forward, but none are able to explain hysteresis completely. [27]

Simple models relating hysteresis to hydrophobic properties (such as the two discussed in Sections 2.3.1 and 2.3.2) were intended to be used on ideal surfaces. For example, surface roughness is not incorporated in Furmidge's model. [30] However, roughness is the only surface property considered by the work of adhesion model. [31] In the former, Furmidge was modeling spray retention in agricultural applications

where the surfaces were smooth and waxed. [4, 27, 30] Regardless, Furmidge's relation (Equation 2.6) has been referenced throughout the literature for regularly patterned (rough) surfaces. [21, 31, 52, 53] The work in this thesis appears to be the first to attempt to apply Furmidge's model to irregularly roughened surfaces.

Chapter 3

Experimental Methods

3.1 Surface Preparation

In the following sections, the methods I used to produce surface roughness are discussed. These techniques were chosen due to their effectiveness in roughening steel and how easily they could be applied (in principle) on an industrial scale. The resulting surfaces had irregular roughness features that promoted water repellency.

3.1.1 Sandblasted Surfaces

Sandblasted surfaces were prepared by Cong Cui of the Duan research group (MUN Engineering). Surface textures were generated using a Vaniman Problast micro-abrasive sandblaster. A nozzle with a 1 mm inner diameter was used with 105-354 μm Al_2O_3 blasting media purchased from McMaster-Carr. Blast pressure was kept constant at 100 psi while the nozzle tip was held within 30 mm of the target. Within 20 minutes, a uniform textured surface was produced. A commercially available metal repellency treatment manufactured by Aculon Inc. was applied to increase hydrophobicity. This is a polymer-based coating (applied as an ethanol-based liquid that dries

in air) that increases water repellency by reducing surface energy. Static contact angles measured on the the resulting surface were as high as 145°.

3.1.2 Sanded Surfaces

The first surfaces prepared for this study were roughened using sandpaper. 3 cm × 3 cm × 0.8 mm stainless steel and Teflon tiles were roughened in this manner. Initially, 100 to 1200 grit sandpapers were used to roughen the surfaces. The roughness of these surfaces was not characterized directly. In principle, a profilometer could be used to characterize the roughness of a small area (5 mm × 5 mm). However, because roughness is not uniform, this small area of information could not be used to infer wetting behavior over the entire surface.

The substrates produced with coarser sandpapers had higher contact angles. During preparation, care was taken to sand from many directions in order to randomize surface geometries. After this process the stainless steel surface displayed contact angles near 90°. To increase the substrate's hydrophobicity, it was immersed in Aculon for 20 minutes, and then air dried. This treatment did not need to be applied to the Teflon surfaces because they displayed strong hydrophobic properties immediately after sanding.

3.1.3 Wax Surfaces

Waxed surfaces were prepared using candle wax. Small wax pieces were broken off of a candle and placed in a shallow glass bowl. The wax was then heated in a laboratory oven just to the point that it flowed freely before being poured over 3 cm × 3 cm × 0.8 mm stainless steel tiles. It was then allowed to completely harden before the excess was trimmed from the tile. The resulting surfaces were very smooth and uniform with slight pitting.

3.2 Contact Angle Measurements

To characterize contact angle hysteresis on irregularly roughened surfaces, a contact angle measuring system (DataPhysics OCA 15EC) was used. The instrument consists of a backlit staging area, a syringe liquid dosing system and camera with 6× optical magnification. The system also includes a software suite (SCA 20) that automates the analysis *via* a live view of the droplet, captured by the camera. The software measures both static and dynamic contact angles, as well as many other droplet parameters including droplet volume, base diameter, interfacial surfaces area, and surface tension. The collected images can also be saved for manual analysis. For all of the surfaces studied, droplets of deionized water were used.

Preparing the device for a measurement was simple and only required a few steps. First, a dosing syringe and needle were mounted to the OCA 15EC and their dimensions were entered into the accompanying software. This allowed the system to accurately control the volume of the dispensed droplet and the rate at which it the liquid was dispensed or retracted. The substrate was then placed on the sample stage and the dosing needle was lowered to its surface. Finally, adjustments were made to the camera and back light so that the image of the needle was sharp and well defined in the live software window. Following the completion of these steps, the system was prepared to collect either static or dynamic contact angle data.

3.2.1 Static Contact Angle Measurement

To measure static contact angles on a surface, the droplet was deposited from the syringe by clicking the dispense button. Once the entire droplet was deposited on the surface, the needle was raised above the droplet such that it remained in the camera's field of view. The software then used boundary lines to fit the droplet contour. For

static measurements, two boundary lines are required: one placed at the interface to define the droplet's baseline, and another placed above the droplet to enclose the area to fit the drop contour. The software includes an automatic baseline detection function that attempts to place it automatically. However, the baseline can also be placed manually by the user.

Next, steps were taken to ensure that a contour line could be accurately fit to the droplet. This involved tilting the lens to achieve a better reflection of the drop on the surface, adjusting the illumination brightness to increase the contrast of the drop's silhouette, and focusing the camera to sharpen the image. These steps are critical in achieving the best contour fit. The apparent contact angle, θ_A, can then be fit on the fly by one of five different calculation algorithms: circle fitting, ellipse fitting, Laplace-Young fitting, polynomial fitting, and manual fitting. For the purposes of this work, ellipse fitting was suitable and used for most measurements. Once these parameters were set, they rarely needed to be readjusted for subsequent measurements. The contact angle was then collected by clicking the fit and collect buttons. The software tabulates measurement data in a result window from which it could be exported in various file formats.

3.2.2 Dynamic Contact Angle Measurement

Measuring the dynamic contact angles of a droplet follows a similar process as the static angles, but with a few additional steps. To measure θ_A and θ_R, the droplet volume was modified while a dynamic tracking function fit the droplet's changing contour. The user can define the rate that the function fits the droplet by providing the number of measurements to be taken per second, or by setting the function to operate as fast as the PC will allow (AFAP). The Advancing and Receding Contact Angle (ARCA) procedure allows the user to chose how much volume is added or

removed from the droplet, and the rate at which the device does so.

Once these parameters were selected, the needle was again lowered to the surface and a droplet dispensed. Unlike static measurements, the needle remained in the droplet during the ARCA procedure. Ideally, the droplet should be centred about the needle. If not, the substrate should be re-positioned. This improves the ease and quality of dynamic contact angle measurements. The upper and lower boundary lines are then set as with the static measurements. Dynamic contact angle measurements also require two additional magnification lines, positioned on the needle above the droplet, to assist in calibrating the contour fit and droplet size. To begin the measurement, Dynamic Tracking was selected before beginning the ARCA procedures. The software then collected data while increasing and decreasing the droplet volume. Again, these results were tabulated within the software's result window before being exported for further analysis in other software.

Chapter 4

Dynamics of Droplets on Roughened Surfaces

This chapter describes the results of 345 dynamic contact angle measurements on roughened surfaces in order to quantify hysteresis. We applied simple models (the work of adhesion and Furmidge models presented in Chapter 2 [30,31]) to predict other dynamic wetting behavior on these surfaces. There were many challenges in obtaining consistent data that was truly representative of the droplet-surface interaction. Our initial findings suggested that variables such as contour fitting profiles, drop volume, dosing rate, and measurement rate affected measurement outcomes in adverse ways. This lead us to examine each factor more closely to gauge how each affected the data. These results will help to facilitate better dynamic contact angle measurements in future studies on irregularly roughened surfaces.

4.1 Outline of the Experiment

An example of dynamic contact angle data from one measurement is presented in Figure 4.1 below. A droplet is deposited onto the substrate before its volume is doubled at the selected dosing rate. This is illustrated in the blue region of Fig. 4.1, which highlights the advancing phase of the contact angle measurement. Once the droplet reaches maximum size, its volume is reduced at the same dosing rate until returning the initial size. This is seen in the green region, which highlights the receding phase. The contact angle and volume data come from fitting the drop's contour to a specific shape at predefined measurement rate. To calculate hysteresis, the maximum and minimum contact angles are taken as θ_A and θ_R, respectively. These points should occur at the end of the advancing and receding phases of the measurement, once the liquid-solid interface has reached its maximum size and remains constant for the rest of the measurement.

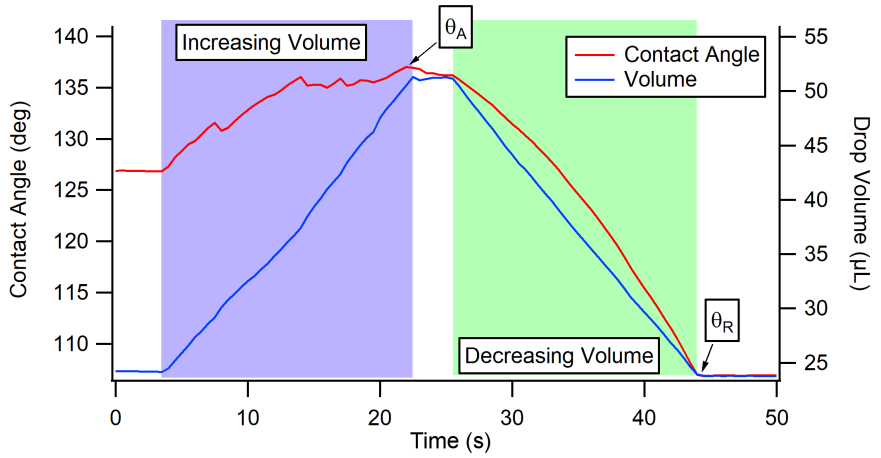

Figure 4.1: Dynamic contact angle and volume measurements on a sandblasted stainless steel surface.

Dynamic contact angle measurements were performed on roughened stainless steel, roughened Teflon, waxed stainless steel, and sandblasted stainless steel samples. A typical dynamic contact angle measurement for each of these substrates is shown in

Figure 4.2.

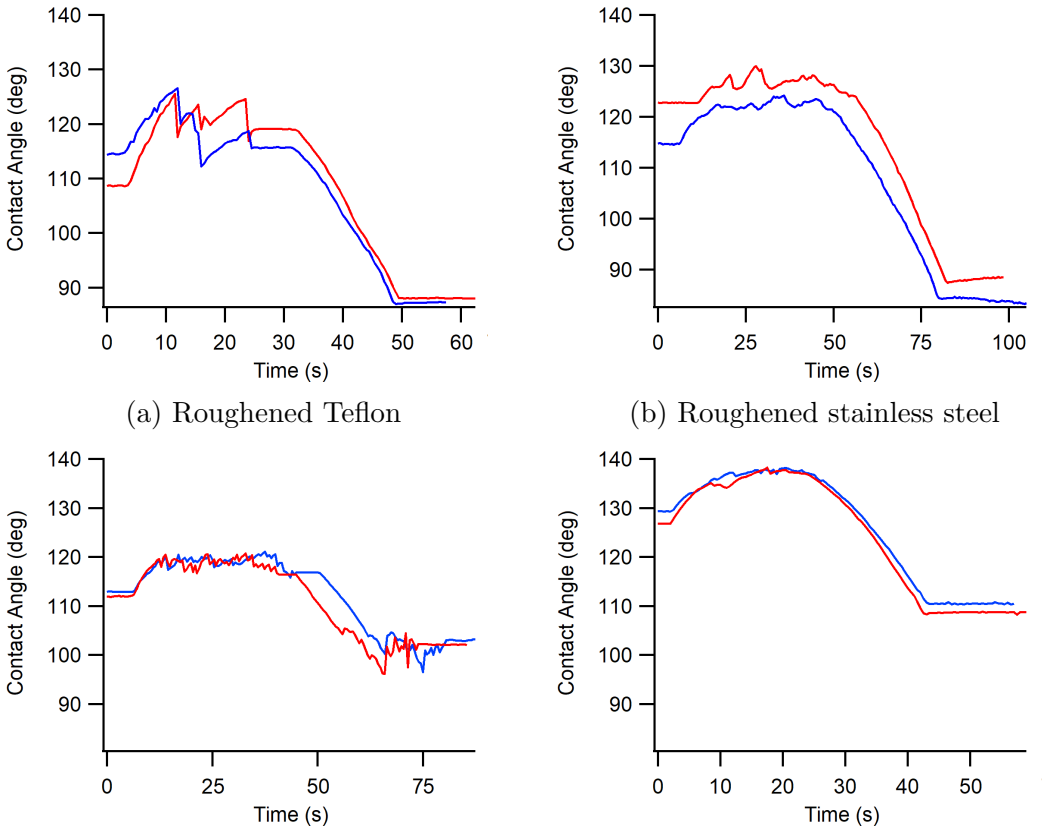

(a) Roughened Teflon

(b) Roughened stainless steel

(c) Waxed stainless steel

(d) Sandblasted stainless steel

Figure 4.2: Two typical dynamic contact angle measurements (red and blue) for tested surfaces. Droplet size was 20 µL, and dosing rate was 2 µL$\cdot s^{-1}$.

4.2 Refining the Dynamic Measurement Method

Initial results from dynamic measurements highlighted the heterogeneity of the surfaces. Contact angles varied by 50° or more for identical volume droplets, and there were many instances of asymmetric droplets forming during the measurements. To study the process of dynamic contact angle measurements and their representation of the physical system, we focused solely on the droplet's size, volume change rate, droplet fitting methods, and the frequency at which fits are applied.

4.2.1 Fitting Methods

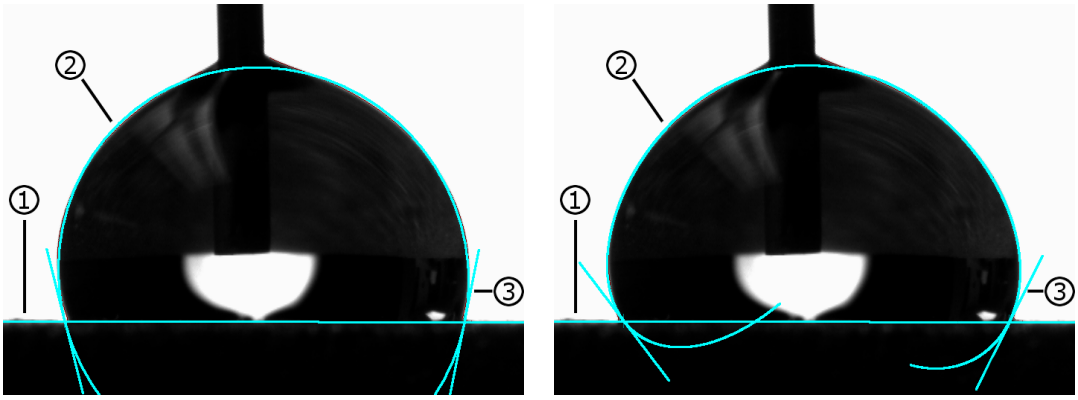

(a) Ellipse fitting (b) Polynomial Fitting

Figure 4.3: Comparison of the baseline (1), contour fit (2), and contact angles (3) produced by elliptical and polynomial fitting of the same droplet during a dynamic contact angle measurement.

We measured contact angles, droplet volume, base diameter, interface area, and other droplet properties by overlaying a selected shape onto the image of the droplet. The software reports how well the overlaid shape fits the drop contour by collecting contour fitting error data. Contour fitting error is not directly related to the contact angle, but indicates how well the software is able to fit the droplet's contour. The difference between the true contour length and the fitted contour length is used to calculate a contour fitting error, with units of μm. For droplets on sandblasted stainless steel, ellipse and polynomial fits appeared most suitable for the droplet contours. An example of each of these fits is shown in Figure 4.3. Other fitting methods available in the software were not used.

To compare fitting algorithms, a video of a dynamic measurement was captured so that each fit could be applied to the same droplet. Both fits (ellipse and polynomial) were then applied to each frame of the video, the results of which are plotted in Figure 4.4. Initially, the polynomial method appears to be better because it is able to measure the contact angles on each side of the drop image independently. This is reflected by

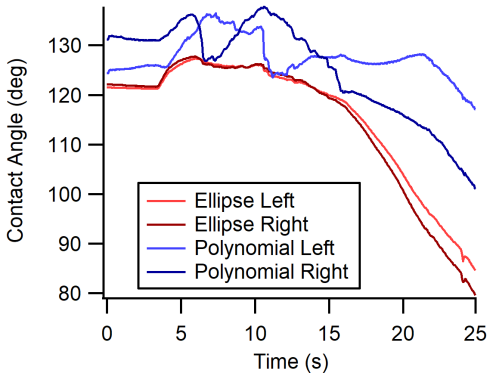

(a) Left and right contact angles.

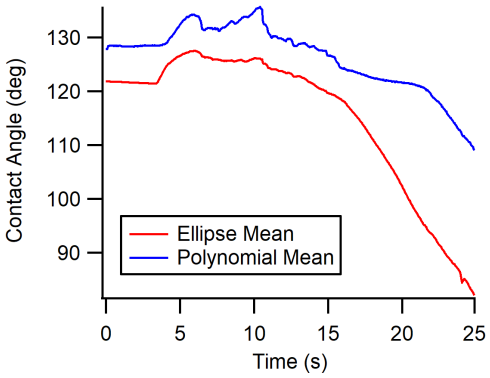

(b) Mean contact angle.

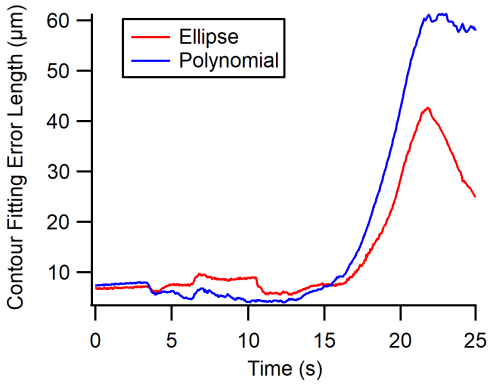

(c) Contour fitting error length of both methods.

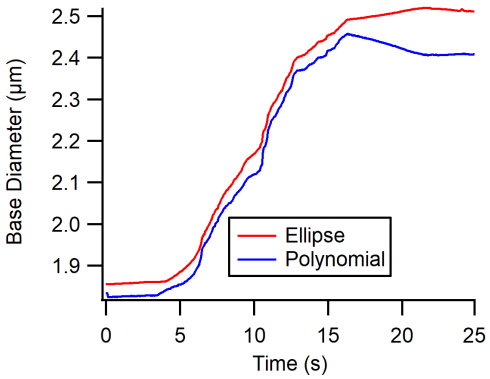

(d) Droplet base diameter.

Figure 4.4: Dynamic droplet characterization using both polynomial (blue) and elliptical fits (red). Droplet volume was initially 20 µL, and increased at with a 2 µLs^{-1} dosing rate, then decreased at the same rate.

the low contour fitting length error values near the start of the measurement (Figure 4.4c). In contrast, the elliptical fit is constrained to have equal left and right contact angles. Otherwise, the fits remain similar as the contact line advances.

During the receding phase, the ellipse fits the drop contour more closely than the polynomial. The polynomial fit is not able to match well the edges of the liquid-solid interface where contact angles are measured, especially where the droplet surface becomes concave. This is shown clearly in Figure 4.5. As evident in Fig. 4.4a, the receding contact angles of the polynomial are approximately 20° greater than those

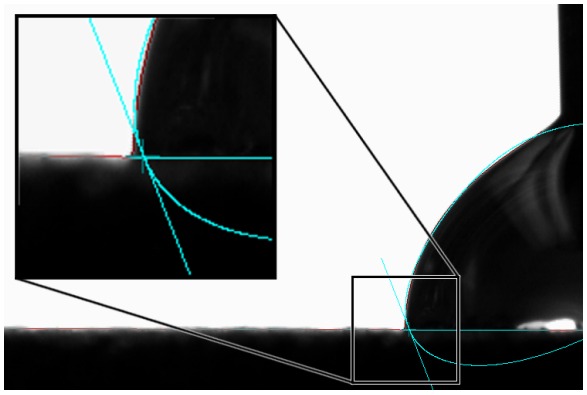

Figure 4.5: Polynomial contour fitting during the receding phase of a dynamic contact angle measurement.

of the ellipse fit.

4.2.2 Asymmetry

Nearly all droplets exhibited asymmetric contact lines during dynamic measurements. When deposited onto the surface, the drops often slid to a pinning site near the needle. The surface would then have to be reoriented so that the needle was centred in the droplet. Once the measurement began, the contact line would usually advance more in one direction. Figure 4.6 shows a droplet that advances preferentially to the right because the left side of the droplet is pinned. In some instances, the advancing direction changed during measurement, signifying that there are multiple strong pinning sites withing a single droplet diameter (2-4 mm).

Evidence of this type of behavior is present in the contact angle results (Figure 4.7). The figure showcases asymmetries at the beginning and end of two measurements in which the contact angle varied by as much as 15° between the left and right sides. Given that the constraints of the elliptical fit tends to minimize the difference between sides, it is possible that the difference was even greater. Contact angle hysteresis is often reported based on the mean contact angle. However, this does not account for

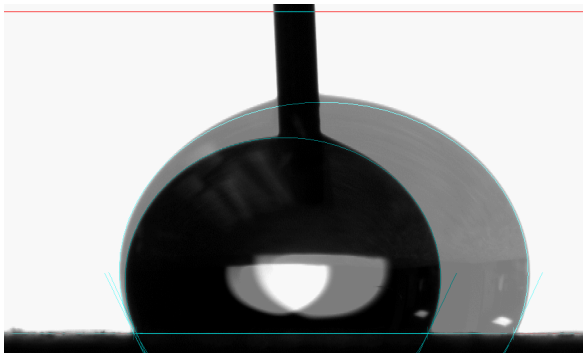

Figure 4.6: Asymmetry of a 20 μL droplet during the advancing phase of dynamic contact angle measurement at a 2 μLs^{-1} rate.

asymmetry. This example shows that taking asymmetry into account would increase the value by 10° or more, which is significant.

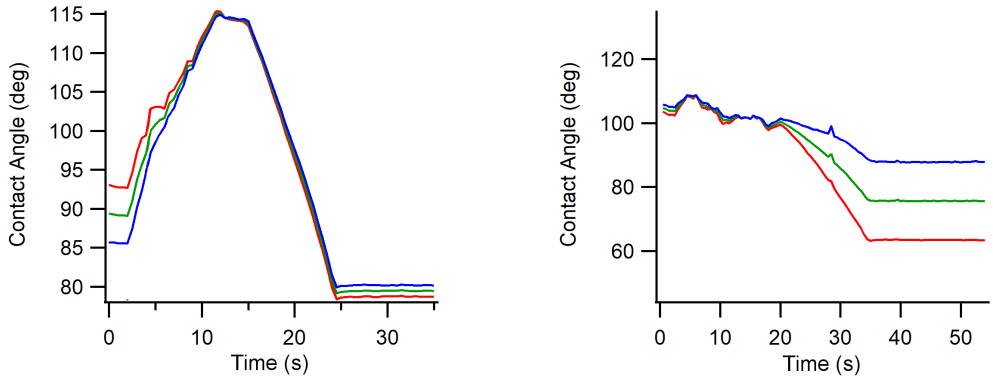

Figure 4.7: Left (red), right (blue), and mean (green) dynamic contact angle measurements representative of 30 μL droplets at a rate of 2 μLs^{-1} with asymmetries occurring at the beginning, (a), and end, (b), of measurement.

The asymmetry of eight droplets was measured by isolated images of the droplet at the beginning and end of the advancing phase. A center line was placed in the images, and from this point, the distance to the left and right contact lines for the initial and final drop sizes were measured. The results from four of these measurements are plotted in Figure 4.8. The difference in left and right contact line expansions ranged from 0.2 mm to 1.1 mm. Of the 8 droplets analyzed, only one of them had the expected

smooth volume data (Fig. 4.8, first row). The expansion difference in the contact line during measurement was 0.6 mm. We found no relation between the asymmetry of the left and right contact angles or the smoothness of the volume change data.

4.2.3 Actual Volume *vs.* Calculated Volume

The droplet's volume change is calculated in the software from the projected area of the contour fit. This presents an opportunity to evaluate the quality of a measurement by comparing the calculated volume change data to the actual droplet volume based on the known dosing rate. This approach is not described in the literature, but we found it very helpful for identifying when catastrophic sever droplet pinning occurs.

For all dynamic measurements, the volume change and dosing rates were the same in the advancing and receding phases. During a measurement, the droplet's volume was increased at the set dosing rate until the droplet increased to the maximum volume specified by the user. After a 2 second pause, the receding phase was induced by retracting the same liquid volume until the droplet returned to its initial volume. Given these parameters, we expected the calculated volume change to be smooth and symmetrical about the droplets maximum size, and initial and final volumes nearly equal (Figure 4.9a). We used this as a criterion to check the quality of dynamic data sets. If the calculated volume changes were not accurate, then we knew that contact angles and other measured parameters were not reliable.

As an example, Figure 4.9b contains irregular dips and peaks which are not representative of the droplet's true contact angle dynamics. The contour fits did not capture the droplet's shape well, so the resulting data was not used in our analysis.

To demonstrate how the calculated volume data compares to the contour fitting length error reported by the software, we applied our volume change criteria to 345 measurements. The measurements were sorted into groups of acceptable and unac-

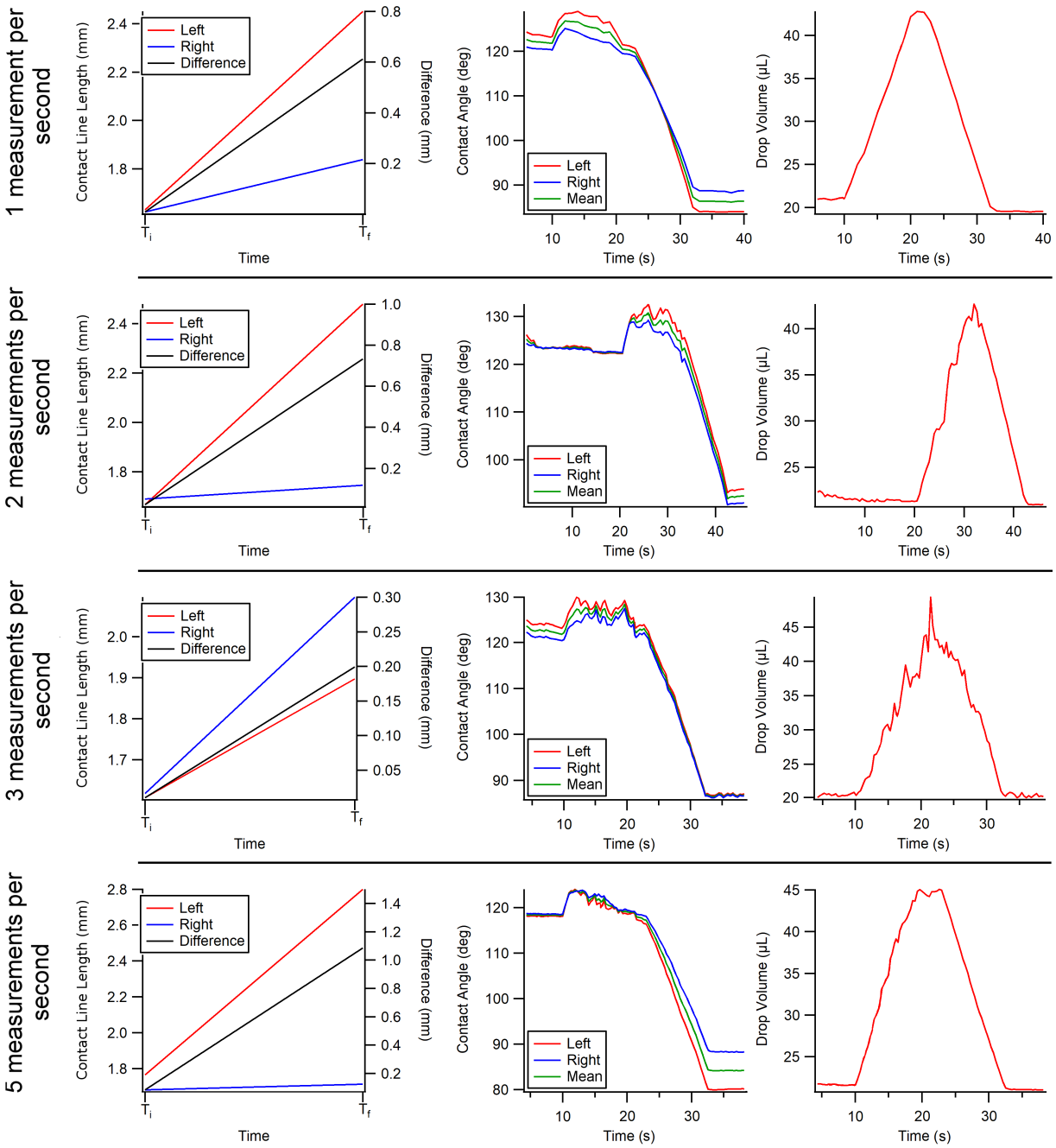

Figure 4.8: Left and right contact line positions (left column), contact angles (centre column), and volume data (right column) for 20 µL drops dispensed at 2 µLs^{-1}. Measurement rates vary from 1 (top row) to 5 (bottom row) measurements per second.

ceptable data sets based on our threshold for a smooth volume change fit. A histogram of the root-mean-square of contour fitting length error data, sorted as acceptable or

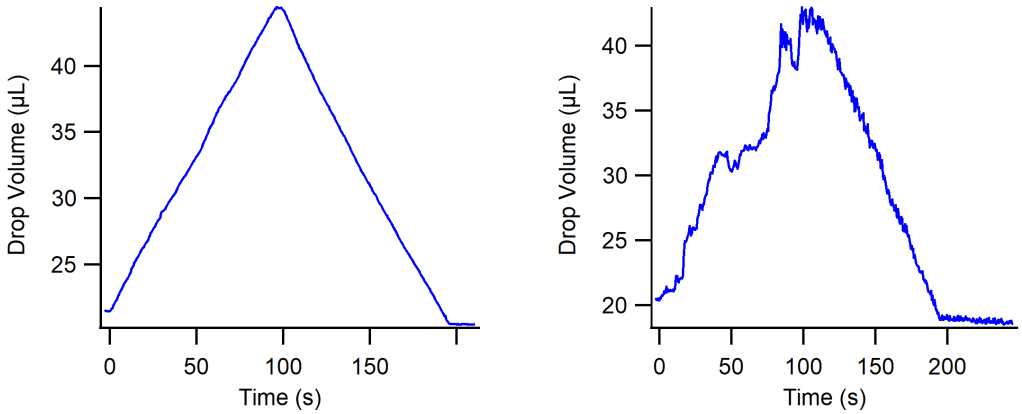

(a) (b)

Figure 4.9: Calculated volume change (blue) of two different representative 20 µL drops during dynamic measurements with a volume change rate of 0.2 µLs^{-1}. (a) shows a good fit (smooth volume changes), while (b) shows a bad fit.

unacceptable, is shown in Figure 4.10. While it is apparent that the acceptable data sets have small RMS contour fitting errors, some unacceptable data sets can also have comparatively low contour fitting error values. Based on this result, we concluded that that the contour fitting length error is not helpful for identifying problems with droplet fits. Thus, we relied exclusively on volume change fit smoothness to identify acceptable data sets.

4.2.4 Measurement Rate

As discussed in Section 3.2.1, the software allows the user to define a set measurement rate. We suspected that this rate could greatly affect dynamic data and how well the droplet is fit by the software. Dynamic contact angle measurements were made using measurements rates from 1-5 s^{-1}, 10 s^{-1}, and using an as-fast-as-possible (AFAP) setting.

To quantify the effect that measurement rate has on the data we compared these results using the volume data standards established in Section 4.2.3. From Table

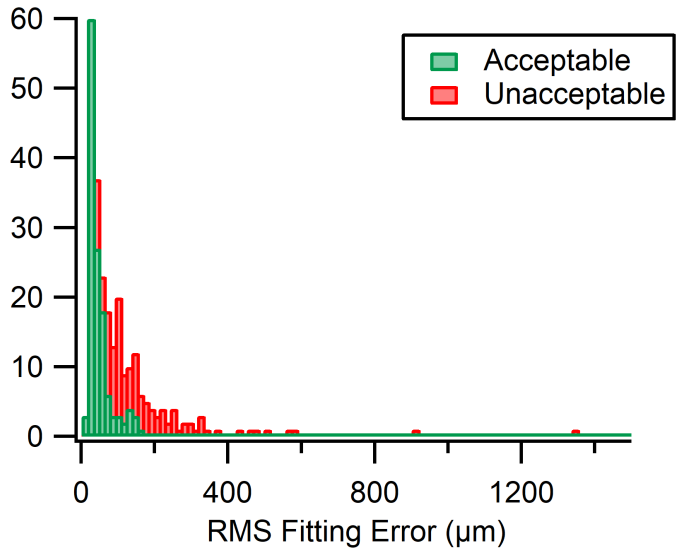

Figure 4.10: Histograms of RMS contour fitting error from acceptable and unacceptable dynamic contact angle measurements.

4.1, we find that data sets collected with measurement rates of 1 s^{-1} and 2 s^{-1} were more frequently acceptable than those collected at higher rates. The true maximum measurement rate was about 6 measurements per second, so 5 s^{-1}, 10 s^{-1}, and AFAP rates were equivalent. We also found that the data fitting rate is not well correlated with the magnitude of error in the length of the contour fit.

Rate (s^{-1})	Acceptable	Total	%
1	7	15	48
2	106	252	42
3	2	15	13
4	3	15	20
5	4	15	27
10	3	15	20
AFAP	4	15	27

Table 4.1: Comparison of acceptable measurements, as a function of data fitting rates, during dynamic CA measurements.

4.3 Dynamic Measurements on Irregularly Roughened Surfaces

Both the roughened Teflon and sandblasted steel samples exhibited near superhydrophobic behaviors. Contact angles observed on these surfaces ranged from 152° to 90° on the Teflon, and from 152° to 105° on the sandblasted surface. The roughened stainless steel samples were less hydrophobic, with contact angles between 134° and 77°. The waxed steel surface was the least hydrophobic, with a maximum advancing contact angle of 123° and minimum receding angle of 96°. This information, along with the mean contact angle hysteresis values for each surface, is tabulated in Table 4.2. The wax showed the least amount of hysteresis despite having the lowest contact angle. Furmidge's relation, Equation 2.6, would predict a lower sliding angle despite having a smaller contact angle. [30]

Surface	Min CA	Max CA	Mean Hysteresis	Mean Predicted SA	Mean Observed SA
Roughened SS	77	134	35	64	60
Sandblasted SS	105	152	27	45	75
Teflon	90	152	24	38	65
Waxed Steel	96	123	13	18	24

Table 4.2: Maximum and minimum advancing and receding contact angles observed, mean contact angle hysteresis, mean observed sliding angle, and mean calculated sliding angle for the tested surfaces. All measurements have units of degrees.

In the literature, static contact angles on roughened, un-coated Teflon ranged from 98° to 126°. [1, 54–56] Stainless steel ranged from 67° (when unaltered) to 94° (when roughened with 320 grit sandpaper). [28, 57] Contact angles between 106° and 134° were reported on ski wax and beeswax surfaces, respectively. [30, 58] The static contact angles from the literature are consistent with our observations for all but the wax surfaces. This may be due to roughness that was present in our wax samples

because of difficulties in melting.

4.3.1 Droplet Size Effects on Sandblasted Stainless Steel

Though most measurements were made using 20 μL droplets, volumes of 5, 10, and 30 μL were also studied. Examples of these measurements are featured in Figures 4.11, 4.12, 4.13, and 4.14.

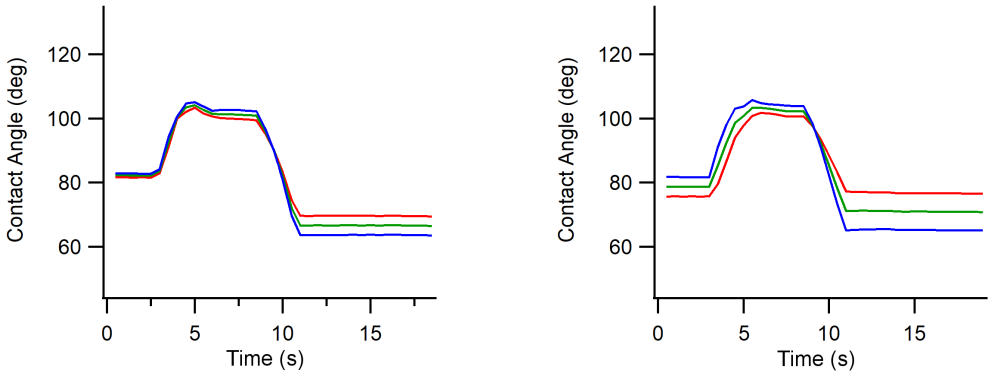

Figure 4.11: Left (red), right (blue), and mean (green) dynamic contact angle measurements of 5 μL droplets, whose volumes were changed at a rate of 2 μLs^{-1}.

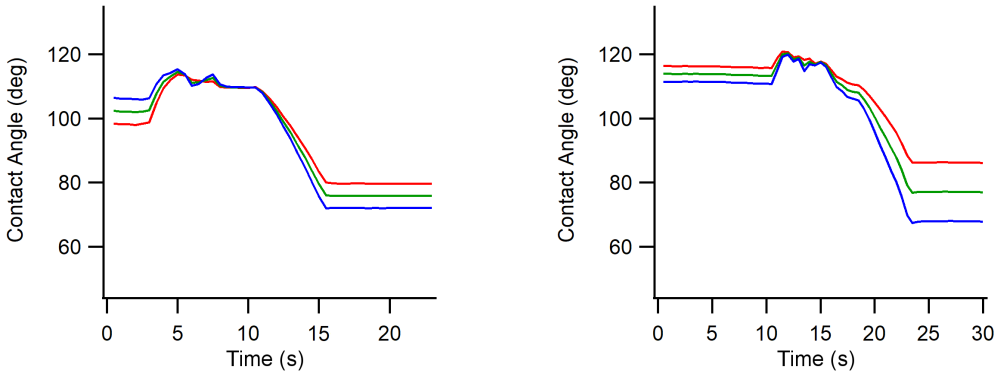

Figure 4.12: Left (red), right (blue), and mean (green) dynamic contact angle measurements of 10 μL droplets, whose volumes were changed at a rate of 2 μLs^{-1}.

Again, using the volume data standards established in Section 4.2.3, measurements collected using smaller droplets had a higher acceptability rate (Table 4.3). We also observed that contour fitting error consistently increases with droplet size.

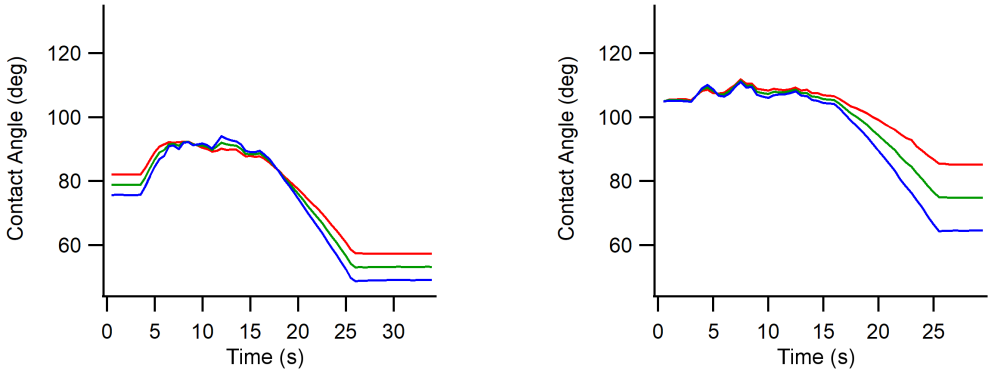

Figure 4.13: Left (red), right (blue), and mean (green) dynamic contact angle measurements of 20 μL droplets, whose volumes were changed at a rate of 2 μLs^{-1}.

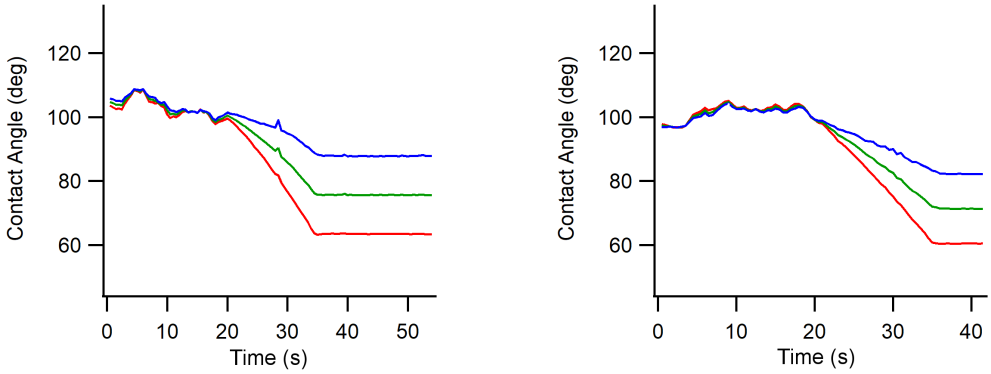

Figure 4.14: Left (red), right (blue), and mean (green) dynamic contact angle measurements of 30 μL droplets, whose volumes were changed at a rate of 2 μLs^{-1}.

Vol (μL)	Acceptable	Total	%
5	25	45	56
10	30	60	50
20	61	180	34
30	14	58	24

Table 4.3: Comparison of droplet volume effects on data acceptability during dynamic CA measurements.

4.3.2 Dosing Rate Effects on Sandblasted Stainless Steel

The speed at which the contact line advances is related to the dosing rate. Throughout these measurements, dosing rates of 1- 3 μLs^{-1} were used. As before, the quality of

measurement results were evaluated using the volume fitting criteria from Section 4.2.3. Table 4.4 suggests that higher dosing rates produced higher quality data, while slower rates did not. This is counterintuitive, since we expected automatic fits to capture a slower advancing contact line better than a faster advancing one (caused by a higher dosing rate).

Rate (μLs^{-1})	Acceptable	Total	%
1	20	73	27
2	77	195	40
3	33	75	44

Table 4.4: Analysis of dosing rate effects during dynamic CA measurements.

4.4 Summary of Findings

This chapter illustrates the many difficulties in measuring dynamic wetting on the randomly roughened surfaces. Of the 345 droplets examined in this study, 133 volume measurements (nearly 60% of all dynamic measurements taken) did not meet the volume data criteria established in Section 4.2.3.

The analysis completed above offers some insight into what affects these measurements and which practices we can now recommend. Ellipse fitting is most suitable for dynamic analysis as it was physically representative (unpinned droplets should be symmetric, and gravity will flatten their shape), and efficient. Of the parameters we examined, drop size had the greatest effect on measurement results. While the contour fitting error tells us how well the instrument is able to fit the perimeter of a droplet, it is not a sufficient indicator of measurement quality. Instead, we recommend using the volume fitting data to evaluate how well the measurements track dynamic droplet changes. A higher dosing rate and lower measurement rate produced

useful data more frequently. Even when using these recommendations to improve measurement outcomes, much of the data was still unusable. We conclude that this is related to catastrophic droplet pinning, which is (unfortunately) a common issue for randomly roughened surfaces.

Chapter 5

Surface Pinning: Looking Ahead

Our measurements of water droplets' contact angle values showed discontinuities during the advancing phase of the measurement. Similar stick-slip phenomena have been reported due to contact line pinning. [59–61] In the coming sections, we propose a new characterization based on this phenomenon. Much of the following discussion is hypothetical, and these findings are preliminary. However, the methods used to measure pinning length scales derived from stick-slip motion are outlined below. Methods to statistically analyze the data are also proposed, and the problems that must be overcome before this characterization can be used are discussed.

5.1 Challenges in Characterizing the Pinning Length Scale

In Chapter 4, the effects of droplet asymmetry, fitting methods, and other measurement factors on data quality were discussed in great detail. From the data we collected, it appears that asymmetric droplet shapes, due to severe surface pinning, cause the discontinuities present in some contact angle measurements. A robust method of

differentiating between contact angle discontinuities due to severe surface pinning, and those due to stick-slip sites, is needed before the characterization methods outlined below can be trusted. Once such a solution is found, the statistical approaches explored in Section 5.3.1 could be applied.

In the remainder of this chapter, data collected from stainless steel samples were used to explore how a characterization based on a surface's pinning behavior could be developed and applied, hypothetically. In the future, it may be possible to characterize a surface in a way that describes the likelihood of a droplet to adhere to the substrate. This would be an important component of predicting water repellency.

5.2 The Effect of Measurement Rate on Discontinuities

Figure 5.1 shows dynamic contact angle data collected from a 20 µL droplet at a sampling rate of three measurement per second. Video frames showing the droplet before and after the base line expansion were isolated so that the droplet's shape could fit manually using image analysis software. Compared to manual measurements, the automatic fit of the droplet's diameter was typically 0.2 mm too large. The contact angles also differed, but they were difficult to measure precisely due to difficulties in viewing the liquid-solid interface in the images.

To observe the true dynamics of the droplet at the surface, additional experiments used screen capture software that compiled animations of the software fitting droplet in real time. The resulting animations were split into frames for analysis. Using the needle's outer diameter to scale the images, it was possible to measure the droplet's contact angles and base diameter manually and compare them to the results from automatic fits.

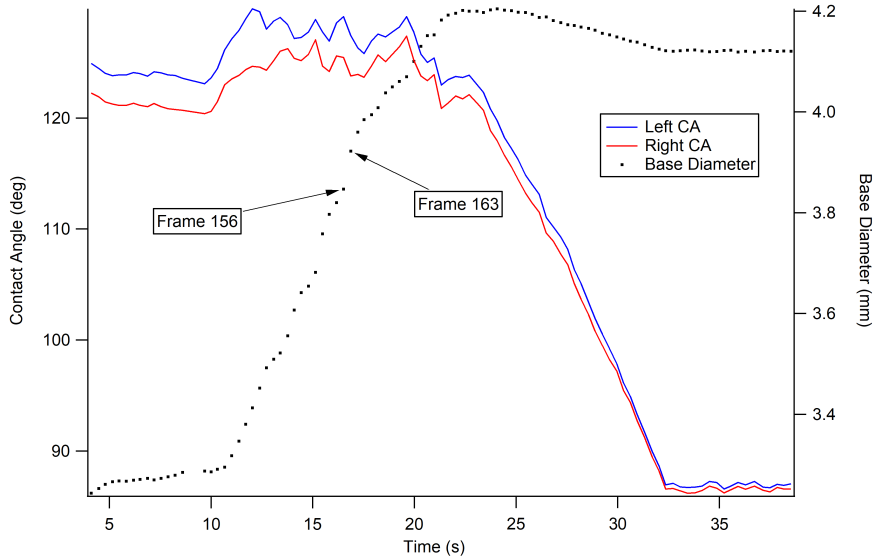

Figure 5.1: Dynamic contact angle and base diameter measurement of a 20 µL droplet. Each point of the base diameter curve was produced by a separate automatic fit to a droplet image extracted from a video.

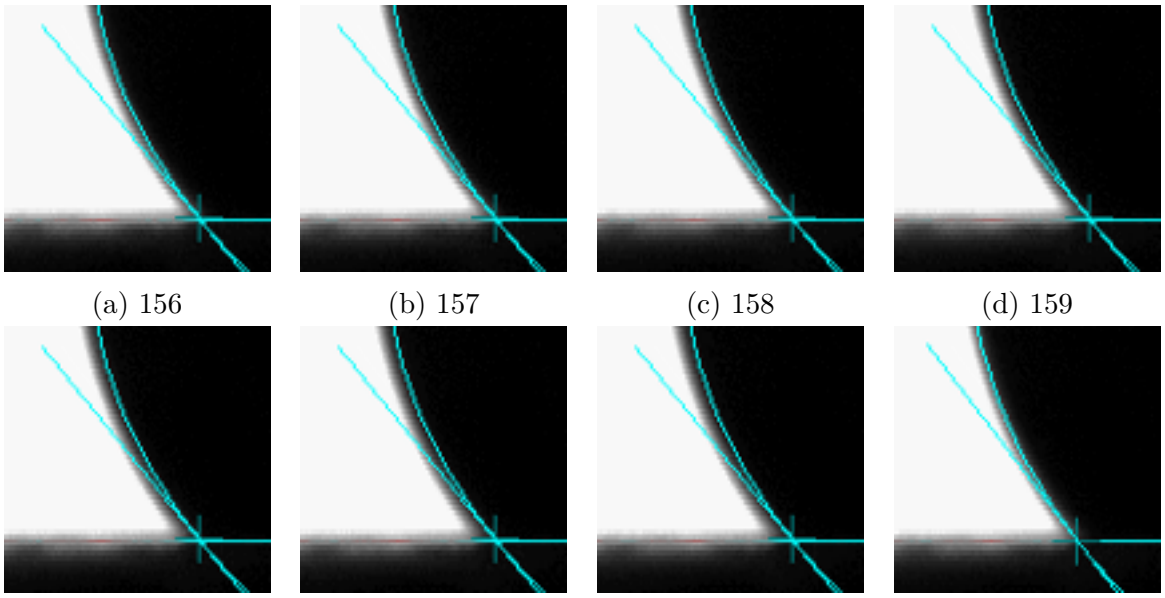

(a) 156 (b) 157 (c) 158 (d) 159

(e) 160 (f) 161 (g) 162 (h) 163

Figure 5.2: Frames 156 - 163 of the dynamic contact angle measurement video data referenced in Figure 5.1. The software's algorithm automatically fits the droplet shape well at frame 156 (a). However, the contact line moves far beyond the fit (b-g) before the next fit is applied at frame 163 (h).

The largest diameter measurement discontinuity in the data set shown in Figure 5.1 occurs at 6.5 seconds. The dynamics of the droplet at this point are captured in frames 156 to 163 of the recorded video, and are depicted in Figure 5.2. These images show that the droplet contact line was advancing much faster than the software was able to fit its shape. This lag results in many large jumps in the automatically fit base diameter and contact angle. Though stick-slip behavior is evident in the video, many of the discontinuities in the contact angle vs. time plots in Figure 5.1 are a result of the automatic fit lagging behind the droplet's rapidly changing size. To solve this problem, we applied manual fitting to each video frame. However, the droplet asymmetry made it difficult to fit the droplets more accurately.

We also measured the dynamics of 20 μL droplets with a much slower dosing rate of 0.2 μLs^{-1}. We expected that using an extremely slow dosing rate would give the software enough time to accurately fit the droplet. However, the results showed little improvement. Thus, issues encountered when fitting a dynamic droplet did stem from large dosing rates.

5.3 Assessing Pinning Length Scales

Slower measurement rates produced better representations of droplet volume. Given that the droplet will expand between automatic fits during dynamic measurements, we expected slow measurement rates to has smaller base diameter changes. Figures 5.3 and 5.4 confirm our suspicions: a faster measurement rate results in smaller base diameter discontinuities.

To illustrate the correlation between a droplet's contact angle and base diameter, measurements of each are plotted alongside each other in Figure 5.5a. Figure 5.5b shows the derivative of the base diameter as calculated by a forward difference scheme.

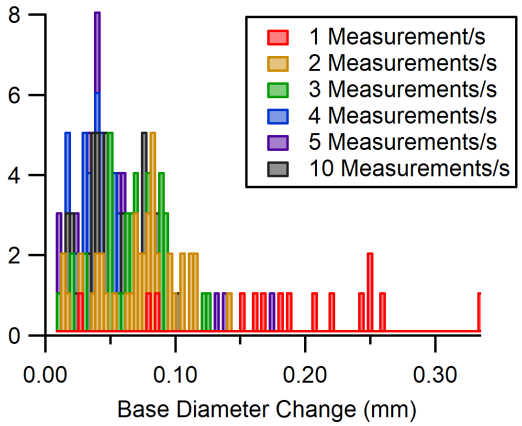

Figure 5.3: Histograms of pinned droplet diameter changes on sandblasted stainless steel for 20 μL drops during dynamic contact angle measurements. Dosing rates were 2 μL·s^{-1}. The measurement rate varied from 1 to 10 measurements per second.

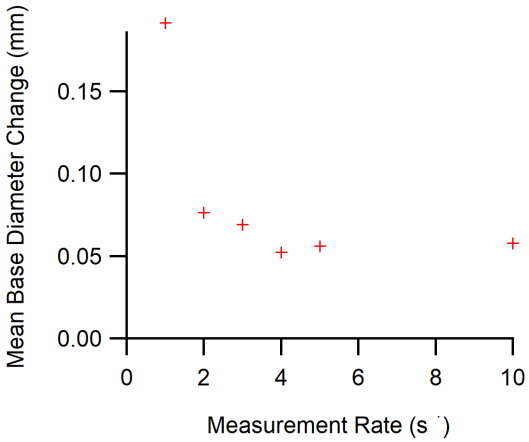

Figure 5.4: The pinned droplet diameter values for 20 μL droplets on sandblasted stainless steel. Dosing rate was 2 μL· s^{-1}, with 1-10 measurements per second.

This yields the rate at which the droplet is changing. The peaks in Figure 5.5b correspond to the discontinuities in the base diameter, which occur simultaneously with peaks in the advancing phase of the contact angle. Thus, taking the derivative of the base diameter data could allow us to quickly calculate its change during stick-slip events. If the contact angle data peaks were solely due to stick-slip pinning (and not severe pinning), then they would indicate the distance between pinning sites on the surface.

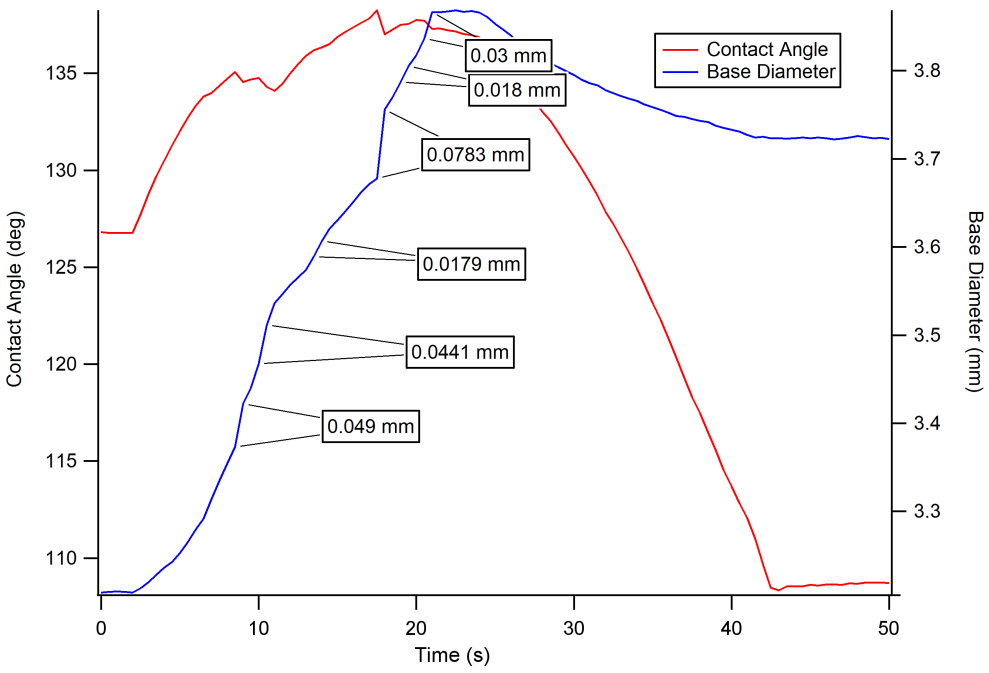

(a) Contact angle (red) and droplet base diameter (blue)

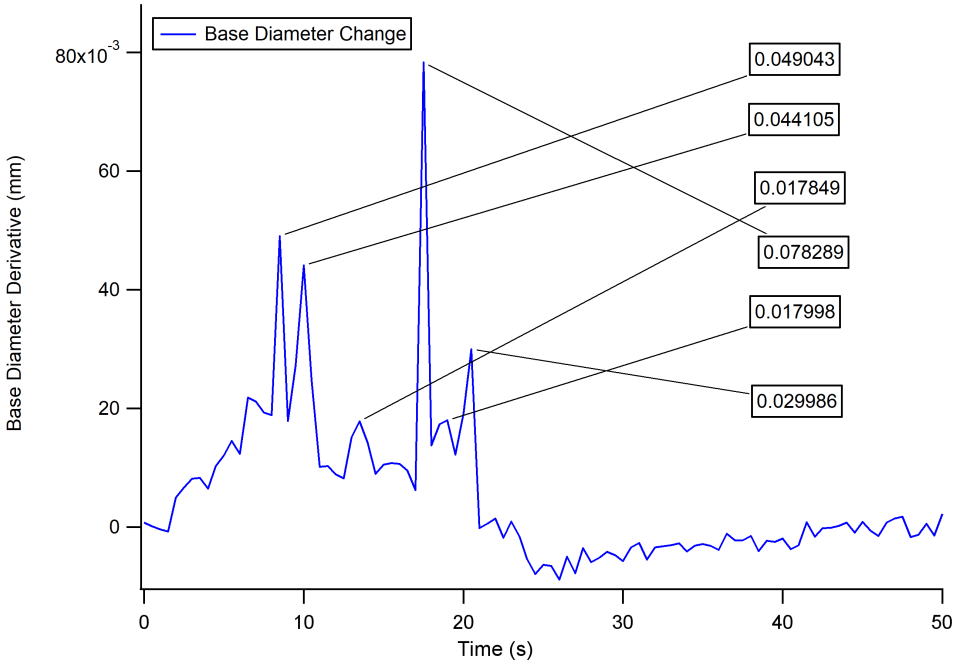

(b) Derivative of base diameter. If the peaks correspond to stick slip behavior then their heights would indicate the distance between pinning sites.

Figure 5.5: Dynamic contact angle measurement of 20 µL drop on sandblasted stainless steel surface, with a dosing rate of 2 µL·s^{-1}.

5.3.1 Presenting Pinning Information

Histograms were used to study trends in the collected base diameter data. By presenting the data in this manner, we can obtain the difference in drop diameter between discontinuities and the frequencies at which they occur. Choosing parameters for the histograms was not trivial. A few approaches were explored to determine how to best present pinning information. Examples of these methods are presented in Figure 5.6.

Histograms were plotted using Scott's Rule (Equation 5.1) to determine the bin widths. [62]

$$w = \frac{3.5\sigma}{n^{1/3}} \tag{5.1}$$

In Figure 5.6, this resulted in the diameters being distributed into thirteen bins starting at the smallest pinning point. Because of the large bin size, much of the data distribution was obscured. It was evident that most diameter changes occurred on small length scales, but further details could not be ascertained.

An alternative set of histograms was produced by dividing the distance between the largest and smallest data points into one hundred bins. As before, the resulting figure shows that pinning occurred on small length scales, because of the additional precision. These histograms were still influenced by bin sizing and offsetting. [62]

Another type of histograms is an average shifted histogram (ASH). These were produced using the University of Alberta's Buriak Group Data Plotter. [62] An average shifted histogram is produced by applying Scott's rule many times to the data set while varying the offset value. The resulting histograms are then averaged to produce a probabilistic curve. This tends to smooth out adverse effects related to bin sizing while retaining significant features in the histogram. The ASH's probabilistic curve highlights the most common drop diameters at which the discontinuities occur. In

the future, this histogram option will allow us to characterize a surface's pinning properties for comparison between different surfaces.

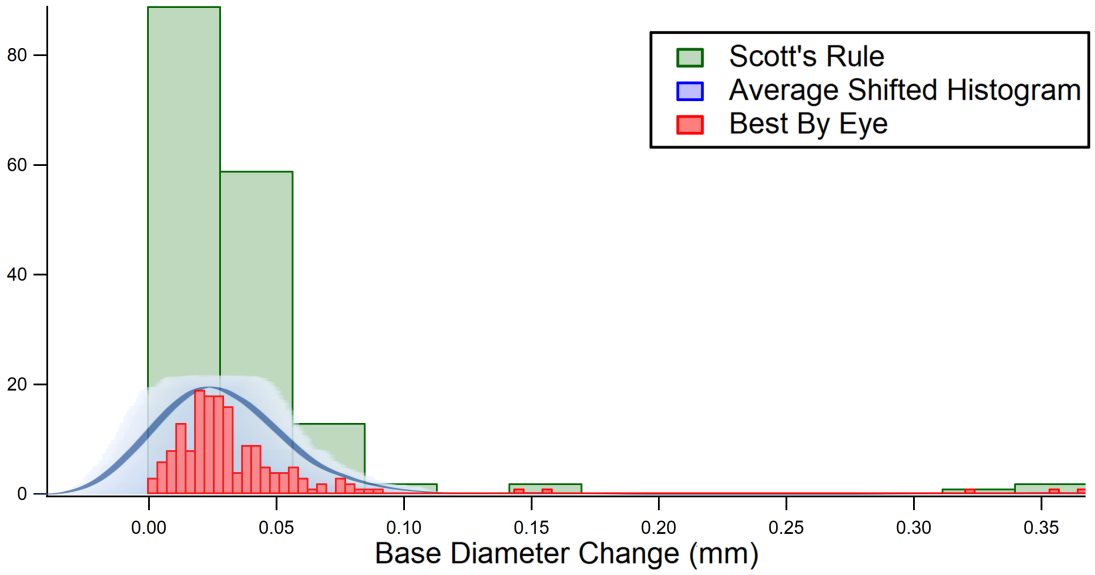

Figure 5.6: Comparison of three histogram methods

Droplet base diameter data collected from a sandblasted substrate is presented as an average shifted histogram in Figure 5.7. It shows that most of the discontinuity features are spaced approximately 40 μm apart. This was unexpected, given that the surface was prepared using much larger particles (105-354 μm Al_2O_3 beads). Though there are small peaks at 100 - 300 μm lengths, we expected that the roughening process did induce some contact line pinning. We do not yet know what causes pinning on this shorter length scale, but some possibilities include roughness features on the original steel surface, or wearing of the Aculon coating.

5.4 Summary

The results presented here help to illustrate how histograms could be used to characterize the pinning characteristics of a surface. In our samples, discontinuities due

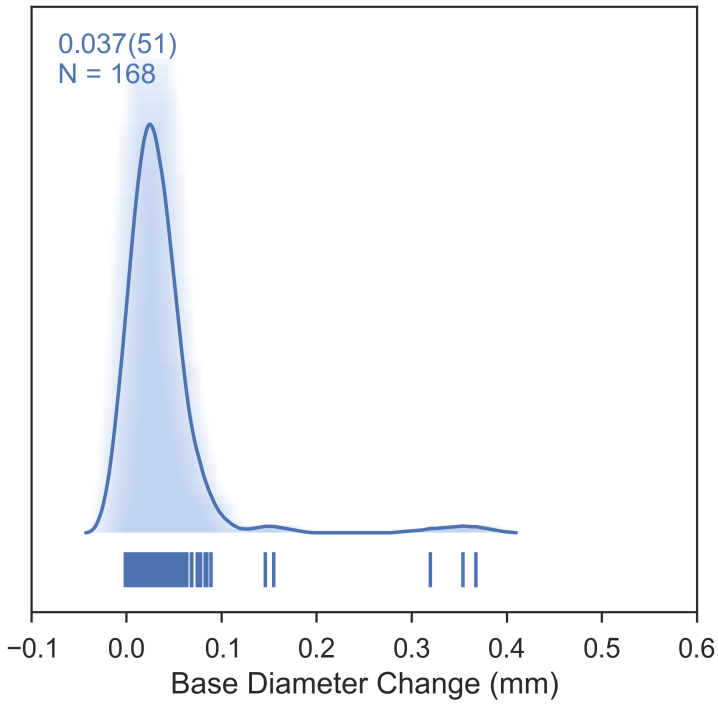

Figure 5.7: Average shifted histogram of pinned droplet diameters on sandblasted stainless steel for a 20 µL drop during dynamic contact angle measurements. The dosing rate was 2 µL·s^{-1}.

to stick-slip behavior are obscured because of severe pinning. Thus, we explored a hypothetical characterization. In future work, this kind of pinning characterization could be used along with static and dynamic contact angle measurements to help identify appropriate hydrophobic and low-adhesion surfaces.

Chapter 6

Conclusions

The findings of this study help illustrate some of the many problems encountered in studying wetting dynamics on randomly roughened surfaces. Droplet shapes on sandblasted surface varied immensely due to severe droplet pinning. Asymmetric drop shapes contributed directly to poor data automatic and manual data fits. This is evident in cases where ellipse fitting (either automatic or manual) was unable to capture the difference between the left and right contact angles. Mention of asymmetric droplets is scarce in the literature so we developed an approach based on volume changes (Section 4.2.3) to evaluate the quality of the data fits. Data quality improved with decreasing drop size. This result is beneficial to those studying realistic systems where small droplets come from precipitation, ocean spray, or other water sources. Other factors, such as dosing and measurement rates, also affected data fit quality. The most accurate fits were attained using higher dosing rates and lower fitting attempt rates.

Wetting behavior of irregularly roughened surfaces, such as sandblasted substrates, was be well described by directly measuring their sliding angles. Nearly all droplets adhered to these surfaces, even though contact angles were very hydrophobic (~150°).

This result could not have been explained Furmidge's model.

Our findings indicate that standard contact angle hysteresis assessments are unsuitable for roughened surfaces with severe pinning. The simple models proposed by Wenzel, Cassie, and Baxter nearly a century ago do not properly account for the severe droplet pinning that can occur with irregular surface features. Likewise, Furmidge's sliding angle model did not predict a reasonable sliding angle for our surfaces. These difficulties were not limited to our sandblasted steel: wetting behavior of other roughened metals and plastics used over the course of this study were not well described by these models. Based on these results, we argue that the field of surface wettability should be less reliant on simplistic models. Though they may work for simple, regularly patterned surfaces they do not account for inning effects, which we find can be severe.

We also proposed an additional stick-slip characterization that would be used alongside static contact angles and hysteresis that is applied in a way that is different from earlier work by others. [59, 63] There would be obvious benefits to knowing a surface's stick-slip behaviour. In water repellency applications, a characterization method based on stick-slip statistics may help greatly to develop better surface treatments. In our future work, we will address the obstacle of differentiating between discontinuities in dynamic contact angle data due to severe droplet pinning through the approaches discussed in Section 5.1. If a solution is found, and we can confidently measure the frequency and length scale of contact line pinning due to stick slip behavior, we can then statistically compare different surfaces.

Appendix A

Equipment Used

A.1 Contact Angle Measuring Instrument OCA 15EC

DataPhysics OCA15 specifications are listed below.

- Measuring range for contact angles: 0-180°; ± 0.1° measuring precision of the video system.
- Measuring range for surface and interfacial tensions: 1×10^{-2} - 2×10^{3} mN/m; resolution: min. ± 0.01 mN/m.
- LED-lighting with manual and software controlled intensity including automatic temperature drift compensation.
- USB 2.0 camera, max. resolution 752 x 480 pixel, max. frame rate 311 frames/s.
- 6-fold zoom lens with integrated fine focus (± 6 mm).
- Field of view: $(1.05 \times 0.66)^{2}$ - (6.72×4.25) mm^2.

- Optical distortion: $< 0.05\%$.

Bibliography

[1] N. J. Shirtcliffe, G. McHale, S. Atherton, and M. I. Newton. An introduction to superhydrophobicity. *Advances in Colloid and Interface Science*, 161(1):124–138, doi:10.1016/j.cis.2009.11.001.

[2] M. Callies and D. Quéré. On water repellency. *Soft Matter*, 1(1):55–61, doi:10.1039/B501657F.

[3] M. Ma and R. M. Hill. Superhydrophobic surfaces. *Current Opinion in Colloid & Interface Science*, 11(4):193–202, doi:10.1016/j.cocis.2006.06.002.

[4] H. B. Eral, D. J. C. M. 't Mannetje, and J. M. Oh. Contact angle hysteresis: a review of fundamentals and applications. *Colloid and Polymer Science*, 291(2):247–260, doi:10.1007/s00396-012-2796-6.

[5] D. Quéré. Wetting and Roughness. *Annual Review of Materials Research*, 38(1):71–99, doi:10.1146/annurev.matsci.38.060407.132434.

[6] T. Xiang, M. Zhang, C. Li, S. Zheng, S. Ding, J. Wang, C. Dong, and L. Yang. A facile method for fabrication of superhydrophobic surface with controllable water adhesion and its applications. *Journal of Alloys and Compounds*, 704(Supplement C):170–179, doi:10.1016/j.jallcom.2017.01.277.

[7] J. Genzer and A. Marmur. Biological and Synthetic Self-Cleaning Surfaces. *MRS Bulletin*, 33(8):742–746, doi:10.1557/mrs2008.159.

[8] H. Zhu, Z. Guo, and W. Liu. Adhesion behaviors on superhydrophobic surfaces. *Chemical Communications*, 50(30):3900–3913, doi:10.1039/C3CC47818A.

[9] P. Roach, N. J. Shirtcliffe, and M. I. Newton. Progess in superhydrophobic surface development. *Soft Matter*, 4(2):224–240, doi:10.1039/B712575P.

[10] K. J. Kubiak, M. C. T. Wilson, T. G. Mathia, and P. Carval. Wettability versus roughness of engineering surfaces. *Wear*, 271(3):523–528, doi:10.1016/j.wear.2010.03.029.

[11] Y. Yuan and T. R. Lee. Contact Angle and Wetting Properties. In *Surface Science Techniques*, Springer Series in Surface Sciences, pages 3–34. Springer, Berlin, Heidelberg, 2013.

[12] J. Genzer and K. Efimenko. Recent developments in superhydrophobic surfaces and their relevance to marine fouling: a review. *Biofouling*, 22(5):339–360, doi:10.1080/08927010600980223.

[13] S. Herminghaus. Roughness-induced non-wetting. *EPL (Europhysics Letters)*, 52(2):165, doi:10.1209/epl/i2000-00418-8.

[14] X. J. Feng and L. Jiang. Design and Creation of Superwetting/Antiwetting Surfaces. *Advanced Materials*, 18(23):3063–3078, doi:10.1002/adma.200501961.

[15] T. Wu and Y. Suzuki. Design, microfabrication and evaluation of robust high-performance superlyophobic surfaces. *Sensors and Actuators B: Chemical*, 156(1):401–409, doi:10.1016/j.snb.2011.04.065.

[16] N. J. Shirtcliffe, G. McHale, M. I. Newton, G. Chabrol, and C. C. Perry. Dual-Scale Roughness Produces Unusually Water-Repellent Surfaces. *Advanced Materials*, 16(21):1929–1932, doi:10.1002/adma.200400315.

[17] Z. Shi and X. Zhang. Contact angle hysteresis analysis on superhydrophobic surface based on the design of channel and pillar models. *Materials & Design*, 131(Supplement C):323–333, doi:10.1016/j.matdes.2017.06.008.

[18] C. W. Extrand and Y. Kumagai. An Experimental Study of Contact Angle Hysteresis. *Journal of Colloid and Interface Science*, 191(2):378–383, doi:10.1006/jcis.1997.4935.

[19] B. Gao and K. M. Poduska. Electrodeposited Zn for Water-Repellent Coatings. *Journal of The Electrochemical Society*, 165(10):D472–D476, 2018.

[20] L. B. Boinovich, A. M. Emelyanenko, V. K. Ivanov, and A. S. Pashinin. Durable Icephobic Coating for Stainless Steel. *ACS Applied Materials & Interfaces*, 5(7):2549–2554, doi:10.1021/am3031272.

[21] X. Yang, X. Liu, Y. Lu, S. Zhou, M. Gao, J. Song, and W. Xu. Controlling the Adhesion of Superhydrophobic Surfaces Using Electrolyte Jet Machining Techniques. *Scientific Reports*, 6, doi:10.1038/srep23985.

[22] E. Bormashenko. Progress in understanding wetting transitions on rough surfaces. *Advances in Colloid and Interface Science*, 222(Supplement C):92–103, doi:10.1016/j.cis.2014.02.009.

[23] B. J. Ryan and K. M. Poduska. Roughness effects on contact angle measurements. *American Journal of Physics*, 76(11):1074–1077, doi:10.1119/1.2952446.

[24] G. Whyman and E. Bormashenko. How to Make the Cassie Wetting State Stable? *Langmuir*, 27(13):8171–8176, doi:10.1021/la2011869.

[25] F. Brochard-Wyart and D. Quéré. Capillary and Wetting Phenomena-Drops, Bubbles, Pearls, Waves. Alex Reisinger, 2002.

[26] L. Gao and T. J. McCarthy. Contact Angle Hysteresis Explained. *Langmuir*, 22(14):6234–6237, doi:10.1021/la060254j.

[27] L. Gao and T. J. McCarthy. Wetting 101°. *Langmuir*, 25(24):14105–14115, doi:10.1021/la902206c.

[28] V. Hejazi, A. D. Moghadam, P. Rohatgi, and M. Nosonovsky. Beyond Wenzel and Cassie–Baxter: Second-Order Effects on the Wetting of Rough Surfaces. *Langmuir*, 30(31):9423–9429, doi:10.1021/la502143v.

[29] Z. Yoshimitsu, A. Nakajima, T. Watanabe, and K. Hashimoto. Effects of Surface Structure on the Hydrophobicity and Sliding Behavior of Water Droplets. *Langmuir*, 18(15):5818–5822, doi:10.1021/la020088p.

[30] C. G. L. Furmidge. Studies at phase interfaces. I. The sliding of liquid drops on solid surfaces and a theory for spray retention. *Journal of Colloid Science*, 17(4):309–324, doi:10.1016/0095-8522(62)90011-9.

[31] Y. Xiu, L. Zhu, D. W. Hess, and C. P. Wong. Relationship between Work of Adhesion and Contact Angle Hysteresis on Superhydrophobic Surfaces. *The Journal of Physical Chemistry C*, 112(30):11403–11407, doi:10.1021/jp711571k.

[32] Y. Liu, S. Li, J. Zhang, Y. Wang, Z. Han, and L. Ren. Fabrication of biomimetic superhydrophobic surface with controlled adhesion by elec-

trodeposition. *Chemical Engineering Journal*, 248(Supplement C):440–447, doi:10.1016/j.cej.2014.03.046.

[33] H. E. Jeong, M. K. Kwak, C. I. Park, and K. Y. Suh. Wettability of nanoengineered dual-roughness surfaces fabricated by UV-assisted capillary force lithography. *Journal of Colloid and Interface Science*, 339(1):202–207, doi:10.1016/j.jcis.2009.07.020.

[34] N. A. Patankar. Transition between Superhydrophobic States on Rough Surfaces. *Langmuir*, 20(17):7097–7102, doi:10.1021/la049329e.

[35] R. N. Wenzel. Resistance of solid surfaces to wetting by water. *Industrial & Engineering Chemistry*, 28(8):988–994, 1936.

[36] K. M. Hay, M. I. Dragila, and J. Liburdy. Theoretical model for the wetting of a rough surface. *Journal of Colloid and Interface Science*, 325(2):472–477, doi:10.1016/j.jcis.2008.06.004.

[37] J. P. Rothstein. Slip on Superhydrophobic Surfaces. *Annual Review of Fluid Mechanics*, 42(1):89–109, doi:10.1146/annurev-fluid-121108-145558.

[38] D. E. Packham. Work of adhesion: contact angles and contact mechanics. *International Journal of Adhesion and Adhesives*, 16(2):121–128, doi:10.1016/0143-7496(95)00034-8.

[39] P. S. H. Forsberg, C. Priest, M. Brinkmann, R. Sedev, and J. Ralston. Contact Line Pinning on Microstructured Surfaces for Liquids in the Wenzel State. *Langmuir*, 26(2):860–865, doi:10.1021/la902296d.

[40] V. Madhurima and K. Nilavarasi. De-pinning of contact line of droplets on rough surfaces. *Journal of Physics: Conference Series*, 765(1):012001, doi:10.1088/1742-6596/765/1/012001.

[41] Y. V. Kalinin, V. Berejnov, and R. E. Thorne. Contact Line Pinning by Microfabricated Patterns: Effects of Microscale Topography. *Langmuir*, 25(9):5391–5397, doi:10.1021/la804095y.

[42] M. A. Sarshar, W. Xu, and C.-H. Choi. Correlation between Contact Line Pinning and Contact Angle Hysteresis on Heterogeneous Surfaces: A Review and Discussion. In K. L. Mittal, editor, *Advances in Contact Angle, Wettability and Adhesion*, pages 1–18. John Wiley & Sons, Inc., 2013.

[43] S. Ramos and A. Tanguy. Pinning-depinning of the contact line on nanorough surfaces. *The European Physical Journal E*, 19(4):433–440, doi:10.1140/epje/i2005-10056-0.

[44] H. Roshan, A. Z. Al-Yaseri, M. Sarmadivaleh, and S. Iglauer. On wettability of shale rocks. *Journal of Colloid and Interface Science*, 475(Supplement C):104–111, doi:10.1016/j.jcis.2016.04.041.

[45] Y. H. Mori, T. G. M. van de Ven, and S. G. Mason. Resistance to spreading of liquids by sharp edged microsteps. *Colloids and Surfaces*, 4(1):1–15, doi:10.1016/0166-6622(82)80085-1.

[46] T. Ondarçuhu and A. Piednoir. Pinning of a Contact Line on Nanometric Steps during the Dewetting of a Terraced Substrate. *Nano Letters*, 5(9):1744–1750, doi:10.1021/nl051093r.

[47] N. L. Abbott, J. P. Folkers, and G. M. Whitesides. Manipulation of the Wettability of Surfaces on the 0.1- to 1 -Micrometer Scale Through Mi-

cromachining and Molecular Self-Assembly. *Science*, 257(5075):1380–1382, doi:10.1126/science.257.5075.1380.

[48] V. de Jonghe and D. Chatain. Experimental study of wetting hysteresis on surfaces with controlled geometrical and/or chemical defects. *Acta Metallurgica et Materialia*, 43(4):1505–1515, doi:10.1016/0956-7151(94)00364-N.

[49] T. Blake and J. Haynes. Kinetics of liquid-liquid displacement. *Journal of colloid and interface science*, 30(3):421–423, 1969.

[50] R. Cox. The dynamics of the spreading of liquids on a solid surface. Part 1. Viscous flow. *Journal of Fluid Mechanics*, 168:169–194, 1986.

[51] O. Voinov. Hydrodynamics of wetting. *Fluid dynamics*, 11(5):714–721, 1976.

[52] L. B. Boinovich and A. M. Emelyanenko. Anti-icing potential of superhydrophobic coatings. *Mendeleev Communications*, 23(1):3–10, 2013.

[53] D. Öner and T. J. McCarthy. Ultrahydrophobic Surfaces. Effects of Topography Length Scales on Wettability. *Langmuir*, 16(20):7777–7782, doi:10.1021/la000598o.

[54] J.-H. Kim, H. P. Kavehpour, and J. P. Rothstein. Dynamic contact angle measurements on superhydrophobic surfaces. *Physics of Fluids*, 27(3):032107, doi:10.1063/1.4915112.

[55] H. Chen, T. Tang, H. Zhao, K.-Y. Law, and A. Amirfazli. How pinning and contact angle hysteresis govern quasi-static liquid drop transfer. *Soft Matter*, 12(7):1998–2008, doi:10.1039/C5SM02451J.

[56] A. Kibar, R. Ozbay, M. A. Sarshar, Y. T. Kang, and C.-H. Choi. Bubble Movement on Inclined Hydrophobic Surfaces. *Langmuir*, 33(43):12016–12027, doi:10.1021/acs.langmuir.7b02831.

[57] S. Nickelsen, A. D. Moghadam, J. B. Ferguson, and P. Rohatgi. Modeling and experimental study of oil/water contact angle on biomimetic micro-parallel-patterned self-cleaning surfaces of selected alloys used in water industry. *Applied Surface Science*, 353(Supplement C):781–787, doi:10.1016/j.apsusc.2015.06.166.

[58] S. Rohm, C. Knoflach, W. Nachbauer, M. Hasler, L. Kaserer, J. van Putten, S. H. Unterberger, and R. Lackner. Effect of Different Bearing Ratios on the Friction between Ultrahigh Molecular Weight Polyethylene Ski Bases and Snow. *ACS Applied Materials & Interfaces*, 8(19):12552–12557, doi:10.1021/acsami.6b02651.

[59] C. Bukowsky, J. M. Torres, and B. D. Vogt. Slip-stick wetting and large contact angle hysteresis on wrinkled surfaces. *Journal of Colloid and Interface Science*, 354(2):825–831, doi:10.1016/j.jcis.2010.11.034.

[60] F. Wang and H. Wu. Molecular origin of contact line stick-slip motion during droplet evaporation. *Scientific Reports*, 5:17521, doi:10.1038/srep17521.

[61] S. Hiltl and A. Böker. Wetting Phenomena on (Gradient) Wrinkle Substrates. *Langmuir*, 32(35):8882–8888, doi:10.1021/acs.langmuir.6b02364.

[62] S. L. Anderson, E. J. Luber, B. C. Olsen, and J. M. Buriak. Substance over Subjectivity: Moving beyond the Histogram. *Chemistry of Materials*, 28(17):5973–5975, doi:10.1021/acs.chemmater.6b03430.

[63] A. Vanossi, G. E. Santoro, N. Manini, M. Cesaratto, and E. Tosatti. Hysteresis from dynamically pinned sliding states. *Surface Science*, 601(18):3670–3675, doi:10.1016/j.susc.2007.07.015.